


Spring 1-1-2018

Numerical Coupling of Fracture and Fluid Pressure Using a Phase-Field Model with Applications in Geomechanics

David B. Culp

University of Colorado at Boulder, davebculp@gmail.com

Follow this and additional works at: https://scholar.colorado.edu/cven_gradetds

 Part of the [Aerodynamics and Fluid Mechanics Commons](#), [Computational Engineering Commons](#), and the [Physics Commons](#)

Recommended Citation

Culp, David B., "Numerical Coupling of Fracture and Fluid Pressure Using a Phase-Field Model with Applications in Geomechanics" (2018). *Civil Engineering Graduate Theses & Dissertations*. 362.
https://scholar.colorado.edu/cven_gradetds/362

This Thesis is brought to you for free and open access by Civil, Environmental, and Architectural Engineering at CU Scholar. It has been accepted for inclusion in Civil Engineering Graduate Theses & Dissertations by an authorized administrator of CU Scholar. For more information, please contact cuscholaradmin@colorado.edu.

**Numerical Coupling of Fracture and Fluid Pressure Using a
Phase-field Model with Applications in Geomechanics**

by

David B. Culp

B.S., Purdue University, 2008

M.S., University of Colorado 2011

A thesis submitted to the
Faculty of the Graduate School of the
University of Colorado in partial fulfillment
of the requirements for the degree of
Master of Science
Department of Civil Engineering

2018

This thesis entitled:
Numerical Coupling of Fracture and Fluid Pressure Using a Phase-field Model with Applications
in Geomechanics
written by David B. Culp
has been approved for the Department of Civil Engineering

Asst. Prof. Mija Hubler

Assoc. Prof. Richard Reguero

Asst. Prof. Jeong-Hoon Song

Date _____

The final copy of this thesis has been examined by the signatories, and we find that both the content and the form meet acceptable presentation standards of scholarly work in the above mentioned discipline.

Culp, David B. (M.S. Structural Mechanics)

Numerical Coupling of Fracture and Fluid Pressure Using a Phase-field Model with Applications
in Geomechanics

Thesis directed by Asst. Prof. Mija Hubler

The application of fracture mechanics is an increasingly important topic in fields including geophysics, geomechanics, materials engineering, structural mechanics and engineering design. Because fracture is a failure mode that occurs on many scales, both temporally as well as spatially, the ability to enlist the help of parallel computation through finite element simulations is important in predicting and modeling these scenarios. Quantifiable measures of failure, such as a material's damage, can be easily computed and tracked when running such simulations. These quantities are not readily available when tests are conducted using physical experiments, nor are their time-scales reasonable for physical experiments, often spanning 10,000's of years in rock-like materials.

This work focuses on the modeling of fracture in saturated, porous materials, and how extreme pore pressures and pressure rates affect the evolution of damage and fluid pressure states. The initiation and evolution of fractures in porous media often gives rise to discontinuous fields within computational problems. Such models present computational challenges due to the complexity of sharp discontinuities that arise during the finite element solution and lack the ability to model fracture initiation. These challenges may be alleviated by using a phase-field formulation of fracture mechanics, which introduces a continuous, diffusive scalar damage field around crack surfaces. We compute the crack's aperture, or crack opening, by making use of the the gradient of the phase-field in the damaged area. This is useful for determining the material's fluid-mechanical properties, such as the estimation of Poiseuille-type flow that occurs within a sufficiently damaged medium.

Using this approach, it can be shown that the evolution of such fractures in a porous medium can contribute to the material's fluid flow characteristics, giving rise to a coupled model of fluid flow and damage within a porous solid. Conversely, the distribution of pore fluid pressures throughout

such a solid, driven by physical processes such as injection or draining, can influence the material's fracture distribution, leading to a model of two-way coupling of damage and fluid flow. Using the Sierra Mechanics code suite at Sandia National Laboratories, a phase-field model of fracture is developed which will allow a loose, two-way coupling of these physics for future implementations. We find the model's ability to predict fractures initiated and propagated by introducing fluid mass to be consistent with analytical solutions. We also find that the crack openings calculated with this model will be helpful for implementing Poiseuille flow along fractures which is a valuable feature in geomechanics modeling.

Dedication

This thesis is dedicated to my family. My wife Alison, and two sons Felix Fox and Lewis Fox have inspired me to pursue this degree in the midst of many challenges in this season of my life. Their love, patience and endless support have given me the endurance to follow through with my aspirations and academic motivations, and engage my passion for learning and scientific pursuit. I have grown as a student, provider, husband and father by taking on this degree over the last several years, and it wouldn't have been possible without you.

Acknowledgements

I would like to thank my adviser, Professor Mija Hubler, for all of her time and effort to help keep this research focused, driven and organized. The way that you invested in me, and encouraged me to follow through with this thesis has taught me to dig deep, and will prove to be a launch-pad into a new and exciting career. Pania Newell has provided so many resources and has been a crucial contributor to this project in both the time she has put forth in hosting my visits to Sandia, as well as all of the advice and answers she has provided regarding mechanics and graduate school. I have also had the pleasure of working with Mike Tupek, of Sandia National Labs, who has provided invaluable input and help with both the coding portions and theory behind this research. Our chats about continuum-mechanics and length-scales have provided much clarity regarding solid modeling. Professors Rich Reguiero and J.H. Song have provided me encouragement, guidance and patience. I am grateful to have worked with you all.

Contents

Chapter	
1	Introduction 1
1.1	Motivation 2
1.2	Deformation, Diffusion and Damage 3
1.3	Literature Review 5
2	Mathematical Formulation of Model 8
2.1	Phase-field Model for Brittle Fracture 8
2.1.1	Energy Minimization 8
2.1.2	Strong Form of Governing Equations 11
2.1.3	Weak Form and Discretization to Galerkin Form 13
2.1.4	Solution Procedure 15
2.1.5	Notes on Phase-field Solution of Fracture 16
2.2	Extension to Saturated Porous Material 17
2.2.1	Fluid Pressures Modify Damage 17
2.2.2	Phase-field Modifies Fluid Pressures 17
2.3	Fluid Mechanics 19
2.3.1	Overview of Sierra/Arpeggio 19
2.3.2	Poiseuille Flow 22
2.3.3	Multiphysics Coupling 23

3	Code Verification	24
3.1	Description of Finite Element Setting	24
3.2	Verification of Model	27
3.2.1	Two-way Coupling	27
3.2.2	Permeability Correction Factor	29
3.2.3	Mesh Convergence Study	30
3.2.4	Analytical Solution of Crack Opening	30
3.2.5	Mesh Alignment Study	35
4	Application and Results	37
4.1	Scope	37
4.1.1	Description of Computational Domain	37
4.2	Geomechanics Setting	39
4.2.1	Problem Description	39
4.2.2	Results and Discussion	41
4.3	Sensitivity of Parameters	44
4.3.1	Motivation and Description	44
4.3.2	Results	46
5	Conclusions and Discussions	50
	Bibliography	52

Tables

Table

3.1	Table of commonly used parameter values	25
-----	---	----

Figures

Figure

1.1	Cartoon of Computational Domain	4
2.1	Phase-field variable, c , around a crack	9
2.2	Anatomy of an Arpeggio Time Step	18
2.3	Flow of Code	21
2.4	Poiseuille Flow	23
3.1	Coarse Mesh	26
3.2	Verification	28
3.3	Correction Factor	31
3.4	Convergence Plot	32
3.5	Crack Opening Benchmark	34
3.6	Permeability Verification	36
4.1	Large Mesh	38
4.2	Injection Illustration with Crack Opening	38
4.3	Flow Rates	39
4.4	Pore Pressure in 3D injection Problem	40
4.5	Phase-field and Crack Opening in Geomechanics Application	43
4.6	Impermeable Injection	45
4.7	Viscosity Sensitivity	47

4.8 Young's Modulus Sensitivity 49

Chapter 1

Introduction

Nomenclature

\mathbf{F}	=	Deformation Gradient	p	=	Fluid Pressure
\mathbf{E}	=	Green Lagrange Strain	κ	=	Bulk modulus
\mathbf{S}	=	Second Piola-Kirchhoff Stress	μ	=	Shear modulus
\mathbf{c}	=	Left Cauchy-Green deformation tensor	Γ^c	=	Damage functional
$\boldsymbol{\sigma}$	=	Cauchy Stress	l_0	=	Fracture length-scale
$\boldsymbol{\epsilon}$	=	Biot Strain	c	=	Phase-field variable
Ψ	=	Strain Energy Density	G_c	=	Critical Energy Release Rate
$\tilde{\Psi}$	=	Positive Strain Energy Density	g, g_p	=	Damage functions
W^+	=	Positive (tensile) strain work	C_r	=	Reaction coefficient
W^-	=	Negative (compressive) strain work	C_d	=	Diffusion coefficient
U	=	Volumetric energy	C_s	=	Source term
\mathcal{H}	=	Maximum elastic energy	ϕ	=	Porosity
Γ^0	=	Fracture surface	μ	=	Dynamic Viscosity
\mathcal{G}_c	=	Critical fracture energy	\mathbf{g}	=	Gravitational Acceleration
k_{eff}	=	Intrinsic Permeability	Q	=	Mass Source
k_F	=	Fracture Permeability	\mathbf{v}	=	Darcy Velocity
b	=	Biot Coefficient	ρ_f	=	Fluid Density
			C_r	=	Rock Compressibility

1.1 Motivation

The coupled physics of pressurized fluids in porous rock and fracture propagation is essential in modeling subsurface rock mechanics. Applications in fields such as hydrology deal with the distributions of contaminants in groundwater, which are often dependent on fracture distributions in the earth's crust, and the phenomenon of fluid induced fault activation is of great interest in the field of geophysics. The concept of carbon sequestration is contingent upon pressurized fluids, and CO_2 being contained within porous solids of the subsurface. In [24] it is shown that under certain pressure conditions, CO_2 and brine will flow along existing joints and faults when an injection occurs at depth. This implies that the CO_2 intended to be sequestered may leak over time.

Because fracture is a failure mode that occurs on many scales, both temporally as well as spatially, the ability to enlist the help of parallel computation through finite elements simulations is important for predicting and modeling these scenarios. Quantifiable measures of failure, such as a material's damage, can be readily computed and tracked when running simulations. These quantities are not readily available when tests are conducted using physical experiments, nor are their time-scales reasonable, often spanning 10,000's of years.

Within this thesis, an overview of the physical processes that are of interest are discussed, followed by a summary of a few methods that are often used to predict fracture, which concludes chapter 1. A review and formulation of the phase-field method is discussed in chapter 2 to familiarize the audience with the material model that was developed for this study is described. A discussion of the mathematical relationship between fluid pressures and fracture culminates with the derivation of the description of solid/fluid coupling. Chapter 3 describes the finite element framework for these studies, and presents a mesh convergence analysis. Comparison of analytical and experimental solutions to the computational results shows the verification of the computational. The 4th chapter presents applications and simulations with the model and chapter 5 provides conclusions and discussion.

1.2 Deformation, Diffusion and Damage

There are three important mechanical properties that are of interest in many subsurface rock mechanics problems: deformation, diffusion, and damage. In porous media these properties are all connected by constitutive relations through the underlying physics. Figure 1.1 depicts how these processes are related. Poroelasticity describes a porous material, with a solid matrix behaving elastically and interstitial fluids that behave viscously. The solid mechanical relations in such a medium are described using the constitutive laws of linear elasticity, and the fluid mechanics with Darcy's law of fluid transport [32]. The three state variables, \mathbf{u} , p , and c , represent displacement, fluid pressure and phase-field damage, and are the primary coupled quantities that are of concern in the boundary value problems described in this thesis.

The first pair of coupled properties that we will consider within a porous solid are damage and deformation. When a solid is deformed, the effective stress within the solid is changed, so long as the surfaces are restrained to limit rigid body modes. When a portion of that solid has reached a critical threshold called the critical energy release rate, or G_c , a crack will propagate [14]. Conversely, when a fracture forms, the elastic strain energy is relaxed, which alters the displacement field of the solid. This coupled model of damage and deformation is formulated here in terms of a damage variable called phase-field.

Using Biot's linear theory of poroelasticity, the processes of fluid flow and fracture within a material can be coupled: the existence of cracks leads to fluid flowing along these joints known as Poiseuille flow, and conversely, an increase in pore pressure, often due to fluid flow, may lead to initiation and/or further propagation of cracks, [5].

It is also important to recognize the coupled mechanisms of fluid transport and displacement within a porous medium, which has already been well established by Terzaghi and Biot in the 20th century, [40]. An example of this is a porous, saturated rock that is not as easily compressed as one that is drained due to the presence of the additional pore pressures in the saturated rock. Biot's model of porosity readily demonstrates the diffusion-and solid displacement.

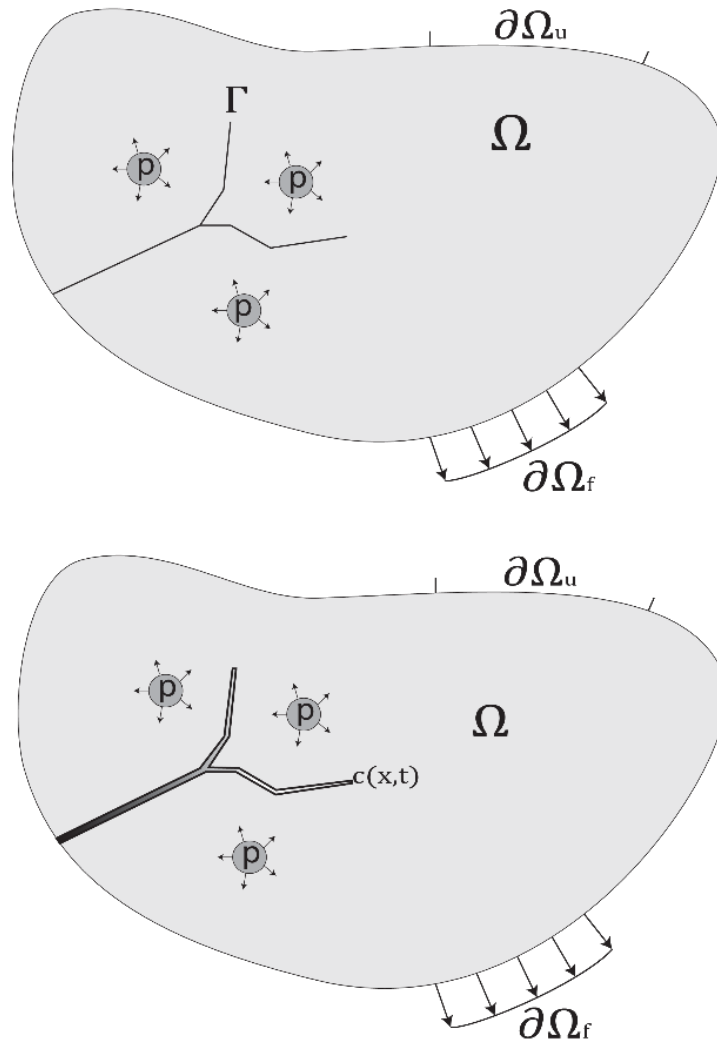


Figure 1.1: A diagram representing a solid body Ω , under traction and displacement boundary conditions, $\partial\Omega_f$ and $\partial\Omega_u$ respectively, with crack surfaces represented as Γ , on the top while the phase-field approximation is represented as $c(\mathbf{x}, t)$ on the bottom. Pore pressure, p , is included as a driving force. The bottom portion of this diagram demonstrates the type of boundary value problem that we focus on in this thesis.

1.3 Literature Review

The importance of understanding damage evolution has led to the development of numerous fracture models, many of which rely on Griffith's theory for brittle fracture, relating a crack's nucleation and propagation to a critical energy release rate. Theoretical fracture models depend on a crack developing or propagating when this critical value is reached, leading to a process zone that transitions from completely undamaged to fully damaged at a single point [7] or over specified region[10].

There are various approaches to numerical modeling of fractures within solids. Of these approaches, several are robust in modeling different fracture scenarios, with reasonable computational expense. The extended finite element method (XFEM), enriches the finite element solution space with discontinuous fields associated with a crack independent of the mesh [29]. However, this approach does not specify the particular physics of fracture initiation and propagation, and implementations in 3D are notoriously difficult due to the complexity of the required computational geometry. In a recent study, [12] describes a model in which XFEM is used to approximate porous flow in fractured media where the fractures are geometrically decoupled from the surrounding porous media.

Another approach is based on the peridynamic theory and assumes that particles within a body interact with each other in a non-local sense, within a finite neighborhood. In this model, fracture occurs as forces acting between material points are decayed to zero based on a predefined threshold, e.g., a critical stretch. The peridynamic equations of motion at a point involve an integral functional of the bond forces in a body. It is a continuum theory, which naturally discretizes as a mesh-free particle method [36]. In this aspect it is favorable over methods that treat cracks explicitly - because the equations of motion and the constitutive models naturally drive fracture initiation and propagation. The use of a pairwise force function is not the traditional method of representing constitutive relations, making the method inconvenient. It is also an oversimplification to assume that any two particles can be simply related with a single force potential [13].

A Lagrangian finite element model for brittle materials based on cohesive zones was developed in the mid 1990's. This method is used to predict the propagation of discontinuities along the interface between elements based on a cohesive traction separation law. These models are a departure from brittle fracture, because cracks may develop from the gradual delamination of the crack surfaces. This process takes place in the cohesive zone, which represents an extended crack tip, and was originally formulated to avoid the crack tip stress singularity that is present in linear elastic fracture mechanics [4]. A major advantage of the cohesive zone model over linear elastic fracture mechanics is the ability to predict behavior of initially undamaged material. A disadvantage to such a method is the mesh-dependency of the fracture path [10]. In [18], a cohesive zone model was developed to simulate dynamic crack growth in saturated porous media, in which cracks are nucleated normal to the maximum effective stress, along with adaptive mesh refinement.

In order to better deal with some of the aforementioned challenges, a phase-field model of fracture is implemented, whose basic motivation is to smooth out the crack surface discontinuity by using a diffusive scalar field, c . Figure 1.1 depicts how a variable, c , approximates a discontinuous function (the crack surface in this case). Since the crack is a natural outcome of the analysis it does not require an explicit geometric representation and tracking, which is an advantage over alternative techniques. This phase-field variable represents damage, and provides a diffuse transition between unbroken and broken material [42]. This damage variable is only defined in the set $[0, 1]$, and will take the value of 0 on the crack surface, while taking a value of 1 away from the crack. For the implementation considered here, we use a fixed mesh to avoid the need for adaptive re-meshing.

Initially put to use in many fields related to material science, the phase-field approach was used to provide a temporally or spatially smooth order parameter, which allowed the effective description of many types of complex microstructure changes such as solidification, and diffusion-controlled phase separation [20]. It is often the case that the discrete phenomena being described by the model are recovered when the characteristic length-scale over which the smoothing occurs is decreased sufficiently. Indeed, the 2008 work of [9] applied a variational approach to the fracture within a body, using an energy functional that closely resembles that which is presented in [30],

which was used in image processing. A phase-field implementation of this functional was later shown to be Γ -convergent as the length-scale approaches zero in [1].

There are several studies in which a coupling of the three aforementioned primary variables of interest are considered. [27], Miehe *et al.* take the approach of crack driving forces, one of which includes fluid pressures. Using a continuum mechanics formulation of the fracture permeability, Miehe models a Poiseuille-type fluid flow that occurs based on deformation in highly damaged areas and is scaled by a characteristic length. Using a different approach as shown in [28], [22], Mikelic and Wheeler use a fully monolithic coupling scheme, solving all PDEs simultaneously, while employing mesh adapting scheme in order to refine without *a priori* knowledge of a crack's location.

In our model development, we use a staggered approach to solve the fluid pressures, p , separately from the tightly coupled displacement and phase-field. We use a continuum approach to calculate a crack's aperture based on the gradient of the phase-field, which is used to update the effective permeability based on a variation of the cubic law from lubrication theory. A correction parameter, γ is specified by the user to properly reflect the roughness of the crack surface upon crack formation and properly adjust the magnitude of the crack opening's effect on permeability. By using the built-in functionality of the Sierra module called Aria, many fluid flow models may easily be implemented using this phase-field implementation such as temperature dependence, gravity, multi-phase flow and unsaturated porous flow [31]. The tests and simulations in this thesis will focus on single-phase porous flow in saturated media.

Chapter 2

Mathematical Formulation of Model

2.1 Phase-field Model for Brittle Fracture

2.1.1 Energy Minimization

We will consider the phase-field formulation which is based on brittle fracture, and use a variational approach to develop the physics of this method. To do this, we must first establish a formulation of the total potential energy and ultimately the Lagrangian of the system, which we wish to minimize for this fracture problem. For a linear-elastic, isotropic material, we consider the elastic strain energy density, $\psi_e(\boldsymbol{\epsilon})$ where $\boldsymbol{\epsilon}$ is the infinitesimal strain tensor, and λ and μ are the Lamé coefficients, as shown below in equation (2.1).

$$\psi_e(\boldsymbol{\epsilon}_{ij}) = \frac{1}{2}\lambda\epsilon_{ii}\epsilon_{jj} + \mu\epsilon_{ij}\epsilon_{ij} \quad (2.1)$$

In equation (2.2), the total potential energy, $\Psi(\epsilon, \Gamma_F)$, is given, which is the sum of the elastic strain energy and fracture energy. According to Griffith, the decrease in strain energy during fracture is balanced by an increase in fracture energy, which can be represented by minimizing the functional in (2.2). $\Gamma_F(t)$ represents a set of crack surfaces that exist within the body at some time t , while Ω is an arbitrary bounded domain [23]. See Figure 1.1 for a visual representation of the arbitrary bounded domain. The fracture energy is calculated by integrating \mathcal{G}_c , the critical fracture energy, over the entire crack surface Γ_F [23].

$$\Psi(\epsilon, \Gamma_F) = \int_{\Omega} \psi_\epsilon d\Omega_F + \int_{\Gamma_F} \mathcal{G}_c d\Gamma_F \quad (2.2)$$

It is convenient to introduce a scalar variable, c , which we will call the phase-field, and a fracture length-scale, l_0 , to develop a regularized formulation of the total potential energy above. By doing so, we can approximate the fracture surface as a crack density functional as shown in equation (2.3). It follows from [26], that this allows us to express the surface integral above as a volume integral as seen in equation (2.4).

$$\Gamma_c = \frac{1}{4l_0} [(c-1)^2 + 4l_0^2 |\nabla c|^2] \quad (2.3)$$

$$\int_{\Gamma_F} \mathcal{G}_c d\Gamma_F \approx \int_{\Omega} \mathcal{G}_c \frac{1}{4l_0} [(c-1)^2 + 4l_0^2 |\nabla c|^2] d\Omega \quad (2.4)$$

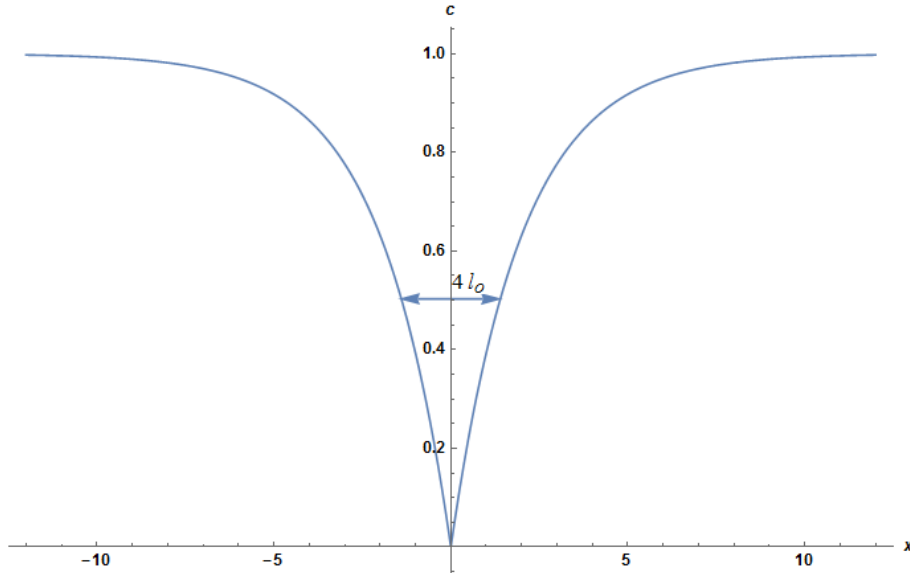


Figure 2.1: Phase-field approximation of a crack in 1-D. The damage parameter, c , portrays a fully damaged material at a value of zero, and is spatially smooth moving away from the crack. The length-scale, l_0 , defines the width over which the crack is smeared.

A user-chosen length-scale variable, l_0 , is introduced which will drive the width over which a fracture is modeled going from $c = 0$, which represents a fully damaged material to $c = 1$,

representing an undamaged state. It is important to note the aforementioned convention being used for damage, c , in this work. In other literature, such as [28] ϕ is used as a similar phase-field variable, while [26] uses the reverse convention for the damage variable d . Figure 2.1 depicts how this scalar variable is distributed around a crack with a given length-scale. [7] show that equation (2.4) can be minimized, when the following Euler-Lagrange equation holds true [23]:

$$c - 1 - 4l_0^2 \Delta c = 0 \quad (2.5)$$

In the case of one dimension, the solution of the differential equation (2.5) leads to the minimization in a single dimension, x :

$$c(x) = 1 - e^{-|x|/2l_0} \quad (2.6)$$

The approximation of equation (2.2) is finalized by considering the form of the elastic strain energy density function, $\tilde{\psi}(\boldsymbol{\epsilon}, \Gamma_F)$. Using Miehe *et al.* as a template, we decompose ψ_e into the tensile and compressive energy contributions, shown as $\psi_e^+(\boldsymbol{\epsilon})$ and $\psi_e^-(\boldsymbol{\epsilon})$ respectively, and assume that the positive elastic strain is decayed by a quadratic damage function. In some implementations of phase-field models, the decay is delayed until a threshold value of the phase-field value is reached, however, we choose to implement the classical phase-field model where the decay begins as soon as non-zero values of phase-field are present. The choice of a quadratic function c^2 is not unique, it simply acts to interpolate between the full contribution of strain energy in the case of a fully intact solid to zero contribution when the material is fully damaged. Indeed, [6] explores a cubic function of damage to more closely reproduce particular stress responses. In this implementation we adopt a quadratic damage function to interpolate the damage state as described in [26].

$$\tilde{\psi}(\boldsymbol{\epsilon}, c) = c^2 \psi_e^+(\boldsymbol{\epsilon}) + \psi_e^-(\boldsymbol{\epsilon}) \quad (2.7)$$

This decomposition effectively removes any crack growth due to compression, which is considered to be a reasonable assumption for fractures, leaving hydrostatic tension and shear as the sole sources of damage. Finally, we can consider our total potential energy approximation, $\tilde{\Psi}$:

$$\tilde{\Psi}(\boldsymbol{\epsilon}, c) = \int_{\Omega} \left[c^2 \psi_e^+(\boldsymbol{\epsilon}) + \psi_e^-(\boldsymbol{\epsilon}) + \frac{1}{4l_0} \mathcal{G}_c[(1-c)^2 + 4l_0 |\nabla c|^2] \right] d\Omega \quad (2.8)$$

In order to impose the irreversible nature of crack growth into our model, a strain-history field, \mathcal{H} , is introduced which satisfies the Kuhn-Tucker conditions for loading and unloading and will replace the tensile contribution of strain energy, ψ_e^+ , when solving for the damage variable. This replacement addresses the idea that c is a monotonically decreasing parameter, and a damaged material will not heal under compressive stresses. This is expressed in equation (2.9):

$$\frac{\partial c}{\partial t} \geq 0 \quad (2.9)$$

Now let us consider the kinetic energy of this arbitrary body:

$$\Psi_{kin}(\dot{u}_i) = \frac{1}{2} \int_{\Omega} \rho \dot{u}_i \dot{u}_i d\Omega, \quad (2.10)$$

where $\dot{u}_i = \frac{\partial u_i}{\partial t}$ is the velocity of the body, and ρ is its mass-density. It is worth noting that we have ignored the dissipative, viscous terms in the micro-force balance equations which is not thermodynamically consistent. On this topic, [8] points out that the local damage model presented is thermodynamically consistent, but not on a global scale due to the solution's dependence on the derivatives of c . Now that we have formulated the potential and kinetic energies of the body, we are able to write the Lagrangian of the fracture problem from (2.8) and (2.10):

$$\mathcal{L}(\dot{\mathbf{u}}, \mathbf{u}, \Gamma_F) = \Psi_{kin} - \tilde{\Psi}_{pot} = \frac{1}{2} \int_{\Omega} \rho \dot{\mathbf{u}} \dot{\mathbf{u}} d\Omega - \int_{\Omega} \left[c^2 \mathcal{H}(\boldsymbol{\epsilon}) + \psi_e^-(\boldsymbol{\epsilon}) + \frac{1}{4l_0} \mathcal{G}_c[(1-c)^2 + 4l_0 |\nabla c|^2] \right] d\Omega \quad (2.11)$$

2.1.2 Strong Form of Governing Equations

Using the Euler-Lagrange equations, we write the governing partial differential equations that describe the problem at hand, whose solutions are minimizers of the energy functional above:

$$\left(\frac{4l_0c\mathcal{H}}{\mathcal{G}_c} + 1\right)c - 4l_0^2\frac{\partial^2c}{\partial x_i\partial x_i} = 1 \quad (2.12)$$

$$\frac{\partial\sigma_{ij}}{\partial x_j} + f_i = \rho\ddot{u}_i \quad (2.13)$$

where \ddot{u}_i represents the second derivative of position with respect to time, and f_i represents the external body forces. As a broad review of the derivation, (2.12) and (2.13) fall out of the Lagrangian energy functional after applying Euler-Lagrange equations [23]. Note that (2.13) is simply a statement of static equilibrium and momentum balance from the classical continuum theory, while (2.12) is a type of reaction diffusion partial differential equation in terms of the gradient of the phase-field damage variable. These equations, which are the strong form equations of motion, can be solved in unison to find the displacement field and phase-field given the following boundary and initial conditions:

$$(BC) \left\{ \begin{array}{l} \nabla \cdot \boldsymbol{\sigma} + \mathbf{f} = \rho\ddot{\mathbf{u}} \text{ on } \Omega \\ \left(\frac{4l_0c\mathcal{H}}{\mathcal{G}_c} + 1\right)c - 4l_0^2\nabla \cdot \nabla c = 1 \text{ on } \Omega \\ \boldsymbol{\sigma} \cdot \mathbf{n} = \mathbf{t} \text{ on } \Omega_h \\ \mathbf{u} = \mathbf{g} \text{ on } \Omega_g \\ \nabla c \cdot \mathbf{n} = 0 \text{ on } \Omega \end{array} \right. \quad (7)$$

$$(IC) \left\{ \begin{array}{l} \mathbf{u}(\mathbf{x}, 0) = \mathbf{u}_0(\mathbf{x}) \text{ on } \Omega \\ \dot{\mathbf{u}}(\mathbf{x}, 0) = \mathbf{v}_0(\mathbf{x}) \text{ on } \Omega \\ c(\mathbf{x}, 0) = c_0(\mathbf{x}) \text{ on } \Omega \end{array} \right. \quad (8)$$

2.1.3 Weak Form and Discretization to Galerkin Form

Using the approach described in [17], we consider the weak form of the described problem, and introduce trial solutions, $\mathbf{u}(t)$, and $c(t)$, with weighting functions \mathbf{w} and q for the displacements and phase-field, respectively, along with their appropriate function spaces as shown below:

$$\mathcal{U}_t = \{\mathbf{u}(t) \in (H(\Omega))^3\} \quad (2.14)$$

$$\mathcal{C}_t = \{c(t) \in H^2(\Omega)\} \quad (2.15)$$

$$\mathcal{W}_u = \{\mathbf{w} \in (H(\Omega))^3\} \quad (2.16)$$

$$\mathcal{W}_c = \{q \in H^2(\Omega)\} \quad (2.17)$$

$$(2.18)$$

where H denotes the class of square-integrable functions, which have appropriate smoothness and are kinematically admissible functions. Integrating by parts and multiplication of our strong form equations by the proper weighting functions yields the weak statement of the problem [7]:

$$(W) \left\{ \begin{array}{l} \text{Given the appropriate boundary and initial conditions, find } \mathbf{u}(t) \text{ and } c(t), \\ \\ \text{such that for all admissible } \mathbf{w} \text{ and } q: \\ \\ \langle \rho \dot{\mathbf{u}}, \mathbf{w} \rangle + \langle \boldsymbol{\sigma}, \nabla \mathbf{w} \rangle = \langle \mathbf{f}, \mathbf{w} \rangle \\ \\ \langle \frac{2l_0 g'(c) \psi^+}{\mathcal{G}_c} + c, q \rangle + \langle 4l_0^2 \nabla c, \nabla q \rangle = \langle 1, q \rangle \\ \\ \langle \rho \mathbf{u}(0), \mathbf{w} \rangle = \langle \rho \mathbf{u}_0, \mathbf{w} \rangle \\ \\ \langle \rho \dot{\mathbf{u}}(0), \mathbf{w} \rangle = \langle \rho \dot{\mathbf{u}}_0, \mathbf{w} \rangle \end{array} \right. \quad (9)$$

where $\langle \bullet, \bullet \rangle = \int_{\Omega} \bullet \bullet \, d\Omega$ is the L_2 inner product over the appropriate domain.

In order to obtain approximate solutions to the boundary value problem, we consider finite dimensional *discretized* trial and weighting spaces, with members $\mathbf{u}^h(t)$, \mathbf{w}^h , $c^h(t)$, and q^h for the

displacements and phase-field. It follows from the previous equations that we are able to formulate the Galerkin form as:

$$(G) \left\{ \begin{array}{l} \text{Given the appropriate boundary and initial conditions, find } \mathbf{u}^h(t) \text{ and } c^h(t), \\ \\ \text{such that for all admissible } \mathbf{w}^h \text{ and } q^h: \\ \\ \langle \rho \ddot{\mathbf{u}}^h, \mathbf{w}^h \rangle + \langle \boldsymbol{\sigma}, \nabla \mathbf{w}^h \rangle = \langle \mathbf{f}, \mathbf{w}^h \rangle \\ \\ \langle \frac{2l_0 g'(c^h) \psi^+}{g_c} + c^h, q^h \rangle + \langle 4l_0^2 \nabla c^h, \nabla q^h \rangle = \langle 1, q^h \rangle \\ \\ \langle \rho \mathbf{u}^h(0), \mathbf{w}^h \rangle = \langle \rho \mathbf{u}_0^h, \mathbf{w}^h \rangle \\ \\ \langle \rho \dot{\mathbf{u}}^h(0), \mathbf{w}^h \rangle = \langle \rho \dot{\mathbf{u}}_0, \mathbf{w}^h \rangle \end{array} \right. \quad (10)$$

We can represent the trial and weighting functions *explicitly* in terms of shape functions $N_A(x)$ and unknown variables d_A , c_A , w_A , and q_A as:

$$u_i^h = \sum_{A=1}^{n_b} N_A(x) u_{iA} \quad (2.19)$$

$$w_i^h = \sum_{A=1}^{n_b} N_A(x) w_{iA} \quad (2.20)$$

$$c^h = \sum_{A=1}^{n_b} N_A(x) c_A \quad (2.21)$$

$$q^h = \sum_{A=1}^{n_b} N_A(x) q_A \quad (2.22)$$

which gives rise to a linear system of n algebraic equations with n unknowns and n_b is the number of nodes [17].

2.1.4 Solution Procedure

The linear elastic phase-field, along with the displacement field, are solved using a time-staggered integration, utilizing an implicit solver for the parameter c and for the momentum balance solution[35].

Within Sierra, an implicit reaction-diffusion equation solver handles the solution of (2.12).

$$C_r = \left(\frac{4l_0 c \mathcal{H}}{\mathcal{G}_c^0}\right) + 1 \quad (2.23)$$

$$C_d = 4l_0^2 \quad (2.24)$$

$$C_s = 1 \quad (2.25)$$

$$(2.26)$$

where C_r is the reaction coefficient, C_d is the diffusion coefficient, and C_s is the source term. The momentum balance equation is handled within Adagio using a nonlinear preconditioned conjugate gradient algorithm to iterate to a converged solution at each time step, which is further covered in [34], [21].

In our material model's implementation of the fracture scenarios to be simulated we use the infinitesimal strain measure, ϵ . Similarly, we choose our stress measure to be Cauchy stress, σ . Upon computation of the displacement field on the mesh the material model updates the strain and stress tensors as:

$$\epsilon = \mathbf{U} - \mathbf{I} \quad (2.27)$$

$$\sigma = c^2 \frac{\partial \psi_e^+}{\partial \epsilon} + \frac{\partial \psi_e^-}{\partial \epsilon} \quad (2.28)$$

where \mathbf{U} , \mathbf{I} and b are the displacement gradient, identity tensor and Biot coefficient, while ϵ^+ and ϵ^- are the positive and negative (tensile and compressive) portions of the strain tensor. The

calculation of these two quantities follow from [8]. Because the fluid pressures are handled using the Aria module, the pore pressures p are transferred into the Adagio scope for proper updating of the stress in (2.28).

2.1.5 Notes on Phase-field Solution of Fracture

The introduction of the length-scale l_0 does indeed have its downfalls, the most obvious of which is that the scaling of the crack leads to the consequence that the approximation Γ_c may be considered the crack surface itself [26]. This effect is minimized by considering a refined mesh and length-scale in areas where cracks may propagate. Because the length-scale can be considered a material property that dictates the critical stress at which a fracture will propagate, it has been shown that as the length-scale goes to zero, the critical stress, σ_c in the crack tends to infinity, and linear elastic fracture mechanics is recovered [41]. [8] shows the relation below, which relates \mathcal{G}_c , σ_c , l_0 and Young's modulus E :

$$\sigma_c = \frac{9}{16} \sqrt{\frac{EG_c}{6l_0}} \quad (2.29)$$

This relationship tells us that the length-scale is inversely proportional to the square of a material's critical stress, and so length-scale that is four times larger will lead to a critical stress that is half. [43] points out that (2.29) can be reformulated to present l_0 as a material parameter, as shown in (2.30), and concludes that the length-scale parameter should be sufficiently small relative to the material specimen in order to avoid significant errors in the predicted critical force response. Because the Young's modulus E , critical stress σ_c and critical energy release rate \mathcal{H} of a material can be determined through experimental means, such as tensile tests, we can directly compute the material's length-scale as:

$$l_0 = \frac{27EG_c}{512\sigma_c^2} \quad (2.30)$$

2.2 Extension to Saturated Porous Material

2.2.1 Fluid Pressures Modify Damage

This material model modifies the standard phase-field model in two critical ways: 1) the total stress is augmented by the hydrostatic term, and 2) the crack opening vector is computed from the phase-field which will be used to update a material's permeability. The following sub-sections detail these processes.

Because we are considering a two-way coupling between fluid flow and damage, a formulation of how each field is updated from the other must be shown. Let us first consider how the solid mechanics (displacement and phase-field) are modified by the onset of fluid flow within a medium. By solving (2.12) we are able to compute the damage field within the medium, and along with the updated strain tensor (2.27) we can directly calculate the total stress (2.28). When considering a porous, fluid saturated material, equation (2.31), is needed to incorporate the hydrostatic pressure of the fluid filling the pore-spaces to augment the total stress, σ :

$$\sigma = \sigma_{eff} - b \cdot p \mathbf{I} \quad (2.31)$$

where σ is the total stress, σ_{eff} is the effective stress in the solid skeleton, b is the Biot coefficient and p is the fluid pore pressure. Including the hydrostatic pressure in (2.31), performs the task of one half of the two-way coupling of damage and flow, by modifying the total stress as a function of pore pressure, which in turn affects the phase-field c . The second half of the coupling occurs when the permeability is updated as a function of phase-field, which is described below.

2.2.2 Phase-field Modifies Fluid Pressures

Within the framework shown in figure 2.3, functionality has been recently added into the Lamé material library. Notably, a crack opening vector is computed as a field variable over the elements in the model, using the spatial gradient of the phase-field variable. This field variable will allow the computation of Poiseuille-type flow through cracks and will be helpful in coupling

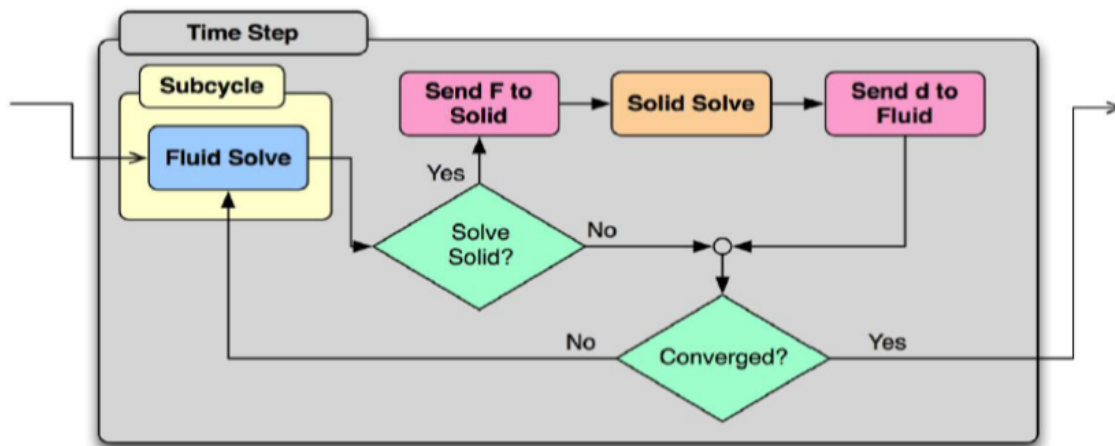


Figure 2.2: A coupled fluid/solid mechanical time step within Sierra showing the fluid/solid convergence cycles. Image courtesy of Martinez *et al.* 2011.

the flow to the solid mechanics portion of the simulation. The crack opening field variable can be summarized by the equations below, in which λ_{\perp} represents the stretch perpendicular to a crack, while ∇c represents the gradient of damage, and \mathbf{C}^{-1} is the inverse of the Right-Cauchy Green tensor in (2.32).

$$\lambda_{\perp}^2 = \frac{\nabla c \cdot \nabla c}{\nabla c \cdot \mathbf{C}^{-1} \cdot \nabla c} \quad (2.32)$$

$$w^2 = \begin{cases} (\lambda_{\perp} - 1)^2 L_{\perp}^2 & c < c_0 \\ 0 & \textit{otherwise} \end{cases} \quad (2.33)$$

The crack opening width represented by scalar w , is formed from a product of the element length in the neighborhood of the crack, L_{\perp} , and an adjusted stretch vector. As (2.33) indicates, this value is zero unless the damage is greater than some user-chosen threshold value, c_0 , which is taken as $c < 0.75$. Ultimately, the crack opening vector $\boldsymbol{\delta}$, the state variable of interest, is formed by scaling the unit vector normal on the deformed crack surface, \mathbf{n} , by the crack opening as shown in (2.34). These equations have been modified from Miehe *et al*'s 2015 work [27].

$$\boldsymbol{\delta} = w\mathbf{n} \quad (2.34)$$

2.3 Fluid Mechanics

2.3.1 Overview of Sierra/Arpeggio

Because we would like to solve for displacements *and* fluid pressures within Sierra, we implement these solutions using two separate modules: Adagio for the solids and Aria for the fluids. Sierra has a tool called Arpeggio that handles the transfer of these fields from one solver to another. After initializing the solid and fluid parameters, a transfer protocol is set up within the input deck, which tells Aria to send the pore pressures to Adagio, and in turn uses the initial pore pressures to update the displacements and phase-field variables in the solid model. After this update occurs,

δ is passed into a user subroutine, which carries out the operation in equation (19), updating \mathbf{k}_f and ultimately \mathbf{k}_{eff} in equation (2.38). The newly updated permeability is then passed on to Aria, which computes the pressure. A pictorial representation of how the different code modules interact is shown in figure 2.3.

The previous subsections have described the pertinent details of our model's implementation within the Adagio model, and now we wish to describe the physics that are handled within Aria. We are concerned with two types of fluid behavior in this model: porous flow, and Poiseuille flow. In the absence of large fractures we consider a porous flow model based on pore pressures and their distributions within a material. Within Aria, the pressures and velocities in such a system are governed by the following general mass balance equation for single phase flow,

$$\frac{\partial \phi \rho_f}{\partial t} = \nabla \cdot (\rho_f \mathbf{v}) + Q \quad (2.35)$$

where the velocity, or flux, can be written in terms of Darcy's law:

$$\mathbf{v} = -\frac{\mathbf{k}}{\mu} \cdot (\nabla p - \rho_f \mathbf{g}) \quad (2.36)$$

where ϕ is porosity, ρ_f is fluid density, \mathbf{v} is the Darcy velocity, Q is a mass source, p is fluid pressure, \mathbf{k} is the permeability tensor, \mathbf{g} is the acceleration due to gravity, and μ is fluid viscosity. For the scope of this thesis we consider this single-phase flow case, with fluid properties of water. For future work we will address more complex flow scenarios, such as two-phase immiscible, water-air mixture, brine and CO₂, which are all readily available within Aria. We also ignore gravitational body forces on the *solid* portion of the domain, while considering them on the fluid mass, so we can more readily focus on the relation between p and the solid mechanical variables. Within Aria's single phase flow regime, we must define either the density or the porosity with a dependence on pressure, and in the case of an incompressible fluid, such as water, we specify porosity as a function of pressure:

Loose Two-Way Loose Coupling of Multi-Physics using Arpeggio

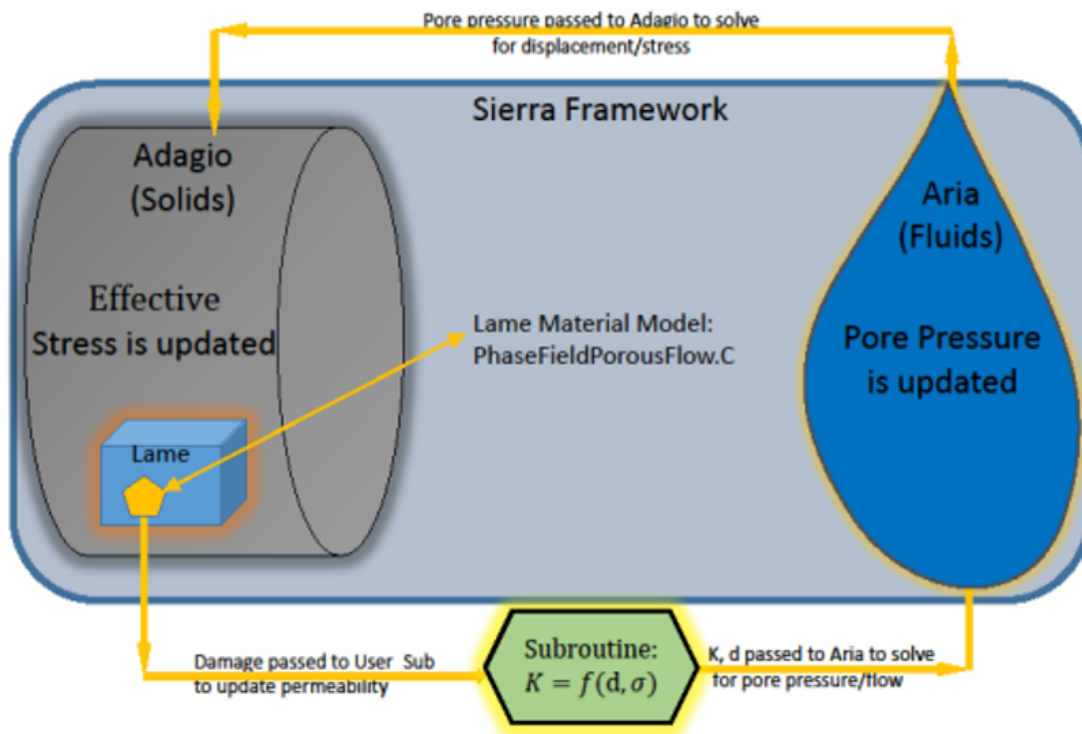


Figure 2.3: A chart which depicts the flow of the code and the different modules within Sierra.

$$\phi = \phi_{ref}[1 + C_r(p - p_{ref})] \quad (2.37)$$

with C_r defined as the rock compressibility, ϕ_{ref} is a reference porosity and p_{ref} as a reference pressure [2]. For our purposes, we define the reference porosity to be our initial porosity $\phi_{ref} = 0.15$ and we take $p_{ref} = 0$ because we neglect any overburden pressures that might arise at depth. In future studies it will be important to define p_{ref} in terms of the depth and the density of the materials above. We calculate a rock compressibility to be a value of $C_r = 10^{-8}$, using Hall's correlation on the initial porosity value [15], which agrees well with other geomechanics values [11].

2.3.2 Poiseuille Flow

In addition to the porous flow that occurs within a poromechanical solid, we also observe fluids that run along pre-existing or newly formed fractures, which is a type of laminar, channel flow called Poiseuille flow. The state variable $\boldsymbol{\delta}$ is essential in our update of the effective permeability across the domain. Using a scheme that blends elements from [24], and [33] we can estimate the modified permeability tensor at any element within the model as a function of $\boldsymbol{\delta}$ using a variation on Poiseuille's cubic law:

$$\mathbf{k}_{eff} = \mathbf{k}_m + \mathbf{k}_f \quad (2.38)$$

where \mathbf{k}_{eff} , \mathbf{k}_m and \mathbf{k}_f represent the effective, intrinsic and fracture permeabilities, respectively. Neglecting gravity effects, we can directly estimate the fracture permeability tensor using our crack opening vector:

$$\mathbf{k}_f = \frac{\boldsymbol{\delta} \cdot \boldsymbol{\delta}}{12\gamma}(\mathbf{I} - \mathbf{n} \otimes \mathbf{n}) \quad (19)$$

where γ is correction factor for the standard cubic law. This factor takes into account a number of physical parameters, namely the roughness of the adjacent surfaces. For future work, this factor should be allowed to adapt by decreasing during the crack opening process, however, this

factor will be held constant for the scope of this thesis. This parameter is easily specified through the input deck and can be used as a measure of ease with which a fluid flows through an open channel, as shown in figure 2.4 and is a topic of model verification in chapter 3 [33]. It should also be noted that \mathbf{n} is the unit normal vector to the crack surface, and the tensor operator $\mathbf{I} - \mathbf{n} \otimes \mathbf{n}$ yields the flux vector when taken as a scalar product with the pressure gradient [38].

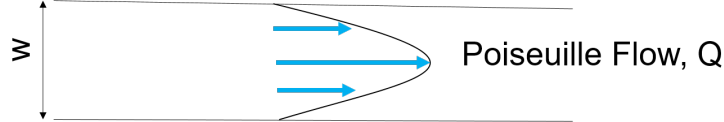


Figure 2.4: Onset of Poiseuille laminar flow through a fracture with crack opening width w

2.3.3 Multiphysics Coupling

As discussed in chapter 1, the flow through porous materials is coupled to solid mechanics through the concept of effective stress: the solid mechanics is connected to the flow by the gradients of pore pressures, while the flow is coupled to the solid mechanics by the material strain's effects on the permeability and porosity fields. Because both the Adagio and Aria compute solutions on a dynamically deforming grid, a coupled accelerating coordinate system must be used, which allows for large deformations. The coupling of Aria's porosity with Adagio's solid displacements is achieved using the following:

$$\det \mathbf{F} = \frac{1 - \phi_0}{1 - \phi} \quad (2.39)$$

which assumes that the solid constituent is rigid, attributing the deformations in the solid skeleton to changes in porosity. The deformation gradient in the equation above is calculated within Aria from the displacements that are transferred in from Adagio. We define p_{ref} and ϕ_{ref} to be a reference pore pressure and porosity, which allows a user defined tolerance to enforce that $\phi - \phi_{ref}$ is reasonable, and if not, p_{ref} and ϕ_{ref} are reset, causing a jump in both fields. This way the solid mechanical deformations computed within Adagio are kept in check with the calculations of the porosity within Aria [24].

Chapter 3

Code Verification

3.1 Description of Finite Element Setting

The numerical models in these studies make use of Sierra Mechanics, developed at Sandia National Laboratories, which is an engineering mechanics simulation framework that has been developed to study computational mechanics using MPI parallel finite element discretization. A variety of rock mechanics problems can be addressed with this suite of codes, and of particular interest to this work is the solid mechanics module called Adagio, and the fluid mechanics module called Aria. Within Sierra’s material library, LAMÉ, a C++ material class called “Phase-field Porous Flow” was created to run simulations for fracture and flow problems, based on a phase-field approach to handle the crack propagation as described in the previous chapter. The preprocessing for all of this work was performed in the software Cubit, while the processing itself was run using a maximum of 80 MPI processors, all controlled remotely. The post-processing software Paraview was used for a bulk of the post-processing in this thesis.

Because we would like to solve for displacements and fluid pressures using separate modules, Sierra has a tool called Arpeggio that handles the transfer of these fields from one solver to another [39]. After initializing the solid and fluid parameters, a transfer protocol is setup within the input deck, which tells Aria to send the pore pressures to Adagio, which in turn uses the initial pore pressures to update the displacements and phase-field variables in the solid model. After this update occurs, the crack opening variables are passed into a user subroutine, which carries out the operation in equation (19), updating k_{eff} . The newly updated permeability is then passed on to

Table 3.1: Table of material, geometric and model parameters used for numerical tests in chapters 3 and 4.

Symbol	Parameter Name	Parameter Value
K	Intrinsic Permeability	$2 \times 10^{-14} \text{ m}^2$
ρ_f	Fluid Density	1000 kg m^{-3}
ρ	Solid Density	2250 kg m^{-3}
α	Biot's Coefficient	1
μ	Dynamic Viscosity	10^{-1} Pa s
ϕ	Porosity	0.15
ν	Poisson's Ratio	0.155
l_0	Fracture Length-scale	0.04 m
G_c	Fracture Energy	100 N/m
C_r	Rock Compressibility	$1 \times 10^{-8} \text{ Pa}^{-1}$
E	Young's Modulus	$30 \times 10^9 \text{ Pa}$
Q, q_0, q_1	Mass Flux	varies
γ	Correction Factor	50
h	mesh length	varies

Aria, which computes the flow with this newly updated permeability information.

The subcycles representing the flow through each time-step are shown in figure 2.2, which includes the convergence criteria for both the Adagio and Aria modules. For the entirety of the remaining numerical tests, a residual tolerance of $1 \cdot 10^{-6}$ was specified for the Adagio convergence, while $1 \cdot 10^{-5}$ was specified for the Aria convergence criteria. Often, the initial time-step would not be sufficiently small for a later time-step to converge.

One of the main difficulties that arises in the solution of such staggered coupling scheme are the sharp transients that arise from the fluids flowing along newly formed fractures. This sort of behavior is well known and is ideally treated with either a semi-implicit scheme or one that is monolithic [19]. To alleviate this, adaptive time-stepping was enabled to ensure the load-step was sufficiently small to satisfy the residual criteria. In particular, Adagio uses a nonlinear preconditioned conjugate gradient solver to handle the quasi-static and implicit dynamic solutions, which is the case for the following problems [25].

It is worth noting that several of the following investigations are similar to those of [27], and [28], which serve as templates for the verification tests. In their studies they make use 2-D quadrilateral elements, while in ours we use 3-D hexahedral elements, often constrained to plane

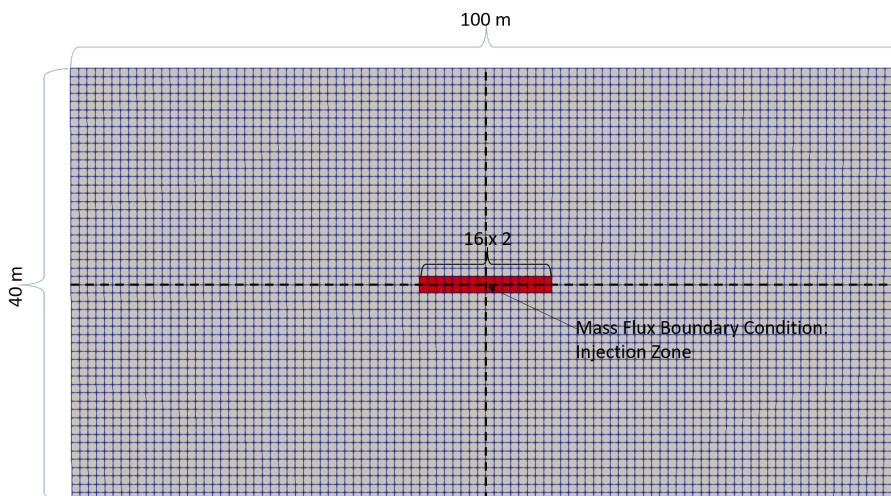


Figure 3.1: Coarse Mesh with $h=1$. The portion in red represents the block where fluid pressures are introduced and crack opening is monitored.

strain conditions. A length scale, $l_0 \approx 2 \cdot h$ suggested in [26] in order to spatially resolve a crack over the span of two elements with mesh parameter h .

The time step is chosen to be 0.01 s unless otherwise noted, although the nonlinear effects of a quicker loading are unnoticed unless using a much more coarse temporal resolution. For all numerical examples during this benchmark, we take $c_0 = 8$ m, $E = 7 \cdot 10^{10}$ Pa, Poisson's ratio $\nu = 0.155$, length-scale $l_0 = 2$ m, $\gamma = 1$, $G_c = 100$ N/m, and solid density $\rho = 2250 \frac{Kg}{M^3}$, which all correspond to values of a typical limestone, represented on a coarse mesh. Table 3.1 lists several of the defining parameters, which have been chosen to represent typical subsurface properties found in many rock types.

3.2 Verification of Model

3.2.1 Two-way Coupling

The following numerical tests serve the purpose of showing that the previously described model produces results that are in line with the physics at hand. The variables that are of special interest to us are the pore pressures p , phase-field c , fracture width w , and the effective permeability tensor \mathbf{k}_{eff} . To keep the computations as inexpensive as possible we enforce quarter symmetry, mesh biasing schemes and plane strain conditions. Three dimensional domains are considered in the applications chapter, and are extensions of the plane strain cases with a sheet of hexahedral elements.

The first property in our code that we wish to test is that the four field variables mentioned above interact and evolve correctly. We would expect that this model properly simulates the connection of them in the following way: in an area with a pressure source, we expect to see increasing pore pressures. The high pore pressures translate to stresses, as indicated in equation (2.28), which drives the phase-field variable to lower values. At the critical value of $c = 0.75$ the material will begin to fracture, at which point the joint opening variable will evolve to non-zero values as shown in equation (2.33) which directly translates to an increase in \mathbf{k}_{eff} . As \mathbf{k}_{eff} increases

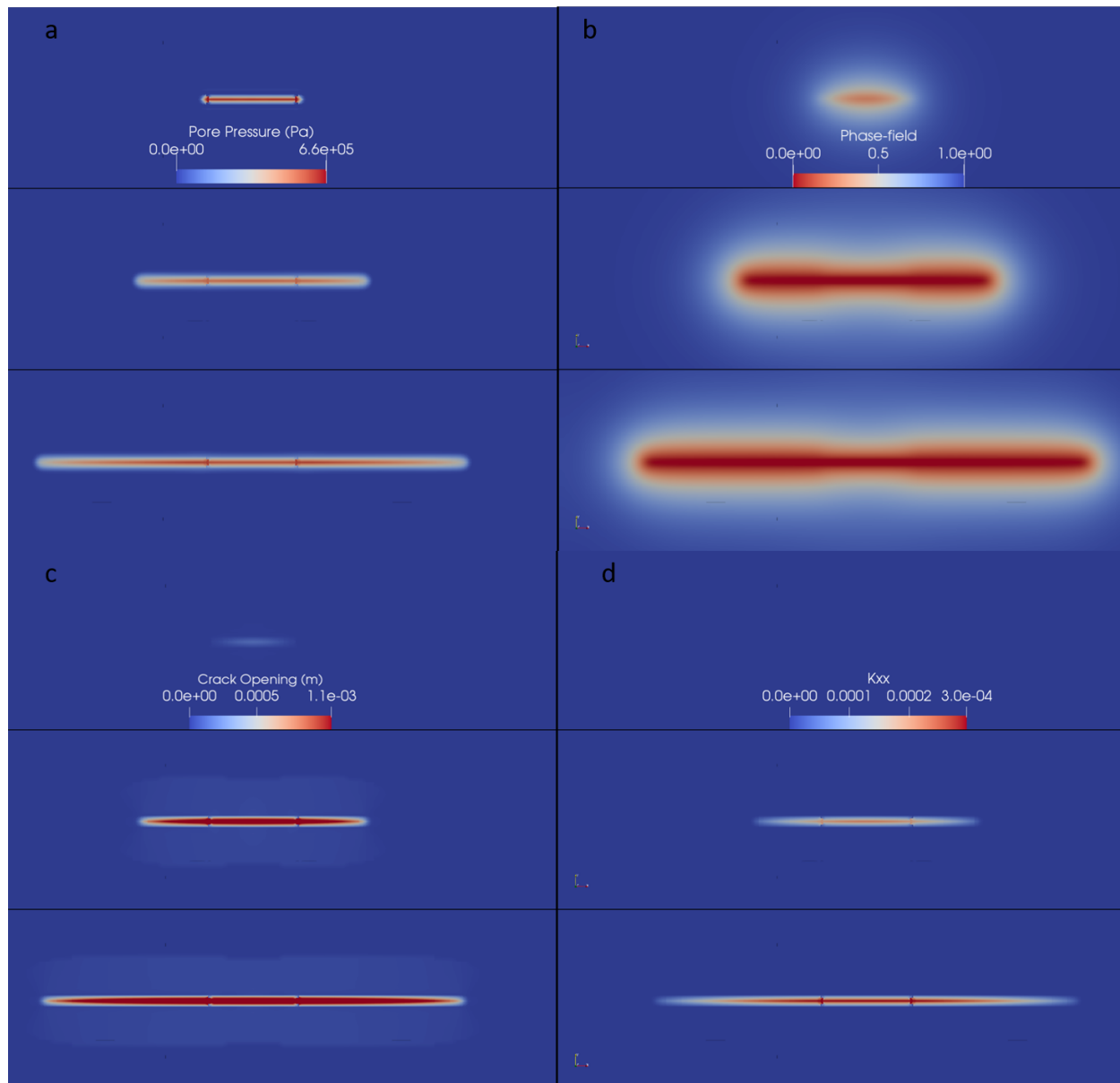


Figure 3.2: **a.** Pore pressure, p shown at times $t = 1.4$ s, $t = 5$ s, and $t = 10$ s. **b.** Phase-field, **c** shown at times $t = 1.4$ s, $t = 5$ s, and $t = 10$ s. **c.** Crack opening, w shown at times $t = 1.4$ s, $t = 5$ s, and $t = 10$ s. **d.** Permeability component, k_{xx} shown at times $t = 1.4$ s, $t = 5$ s and $t = 10$ s. Notice the absence of any discernible permeability at time $t = 1.4$. This is expected because there is not enough of a crack opening at this low of a pore-pressure/damage state.

in the areas adjacent to fluid injection, the fluid will flow into these areas causing increased pore pressures, while at the same time draining the injection area.

We test the physical processes outlined above with a sheet of hexahedral elements in a plain strain configuration as depicted in figure 3.1. The fluid pressure is introduced across the injection surface at a rate of $Q = 0.32 \frac{kg}{s \cdot m^2}$, and the simulation is run for 10 s. The results of the pore pressure, phase-field, crack opening, and permeability component k_{xx} are shown in figures 3.2 a-d, respectively. Each figure shows a snapshot of the respective variable at $t = 1.4$ s, $t = 5$ s, and $t = 10$ s.

As expected, we see the advancement of damage, and diffusion with increasing pore pressures. The two-way coupling is clearly captured in figure 3.2 as the pressures drive damage, and the damaged areas alter the pressure distributions. Of particular interest is the relatively low value of w at $t = 1.4$ s, and the complete absence of k_{xx} at the same time step. We expect this to be the case as the pressures are too low to have caused much damage at this point.

3.2.2 Permeability Correction Factor

The second property that we test is the behavior of the correction factor γ , which is used to control how much w contributes to \mathbf{k}_{eff} . To do this we will monitor the value of \mathbf{k}_{eff} for several values of γ . When $\gamma \gg 0$ we expect there to be very little contribution of fracture to the permeability. With a value of $\gamma_0 \approx 0$ we expect a very large effect and with $\gamma = 1000$ we expect a reasonably physical effect. Using a length scale of $l_0 = 0.5$, we vary the correction parameter from $\gamma = 0.1$ up to $\gamma = 1000$, in a simulation with the same geometry and material parameters as in the prior tests, and compare the crack opening and values of k_{xx} along the crack at $t = 5$ s. Figure 3.3 shows the results.

As we would expect, the crack openings increase in a hyperbolic fashion as the correction factor is increased. Physically, the increased γ leads to a lower permeability, which in turn allows the pore pressures to diffuse slower. The increased pore pressures in the crack mean a higher crack opening displacement. The bottom plot in figure 3.3 shows that the effective permeability will

decrease in a hyperbolic fashion with increasing γ . This is also what we expect, and is directly dictated by equation (19).

3.2.3 Mesh Convergence Study

To ensure mathematical convergence, we choose to monitor the crack opening variable that is calculated from (2.33), while decreasing the element size. Figure 3.1 depicts the domain with the coarsest mesh considered in this study, with size $h=1$, corresponding to 5200 hexahedral elements total, and 32 in the area of the mesh where the fluid pressures are injected. The maximum refinement considered had $h=4.5$, corresponding to 520,000 elements on the mesh, with 3200 of them in the injection zone. The size of the computational domain was 100 m x 52 m x 1 m, while the injection zone was 16 m x 2 m x 1 m in X,Y,Z. Plane strain conditions were enforced on the top and bottom of the mesh, while the +Y and +X sides of the domain were free to displace. Quarter symmetric boundary conditions were set up along the -X and -Y sides, and a mass flux boundary condition introduced fluid pressures at a rate of $2 \cdot 10^5 \frac{Pa}{s}$. The results of the study are shown in figure 3.4, where it is clear that the crack opening magnitude converges to a value, which turns out to be the analytical solution to this problem, as discussed in the next subsection.

3.2.4 Analytical Solution of Crack Opening

In [37] several analytical solutions of a pressurized crack's aperture are derived using Griffith's fracture criteria. These solutions cover different scenarios such as circular cracks and fractures under plane strain assumptions. Sneddon's analytical solution for the crack opening width is shown to be:

$$w = 2||\delta|| = \frac{4 \cdot (1 - \nu)^2 c_0}{E} \quad (3.1)$$

which leads to their solution of:

$$w(x) = \frac{4 \cdot p \cdot c_0 (1 - \nu^2) (1 - \frac{x^2}{c_0})^{\frac{1}{2}}}{E} \quad (3.2)$$

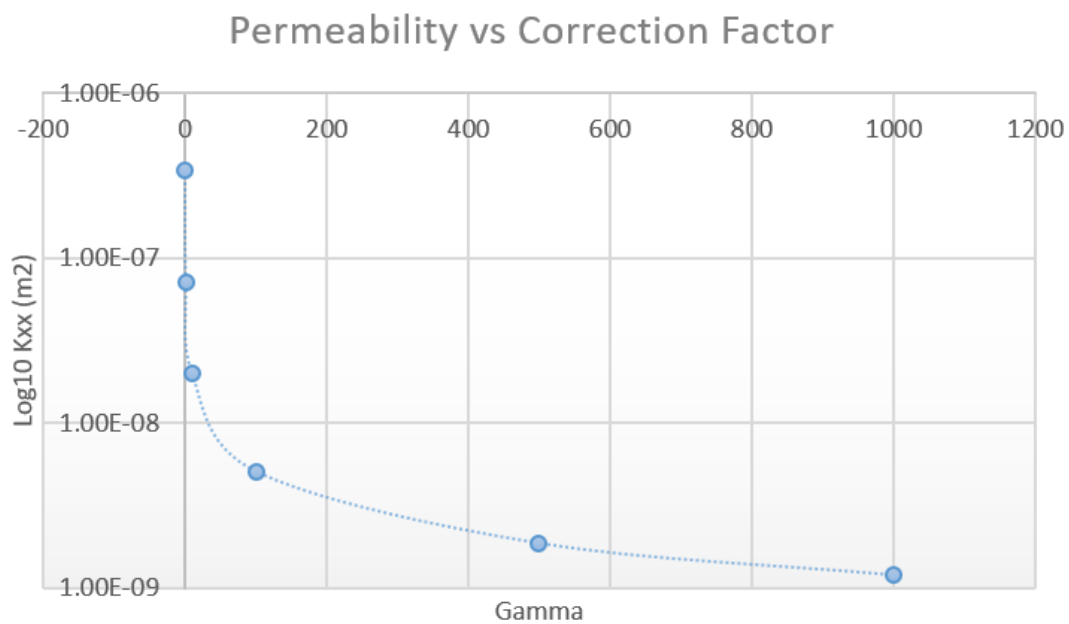
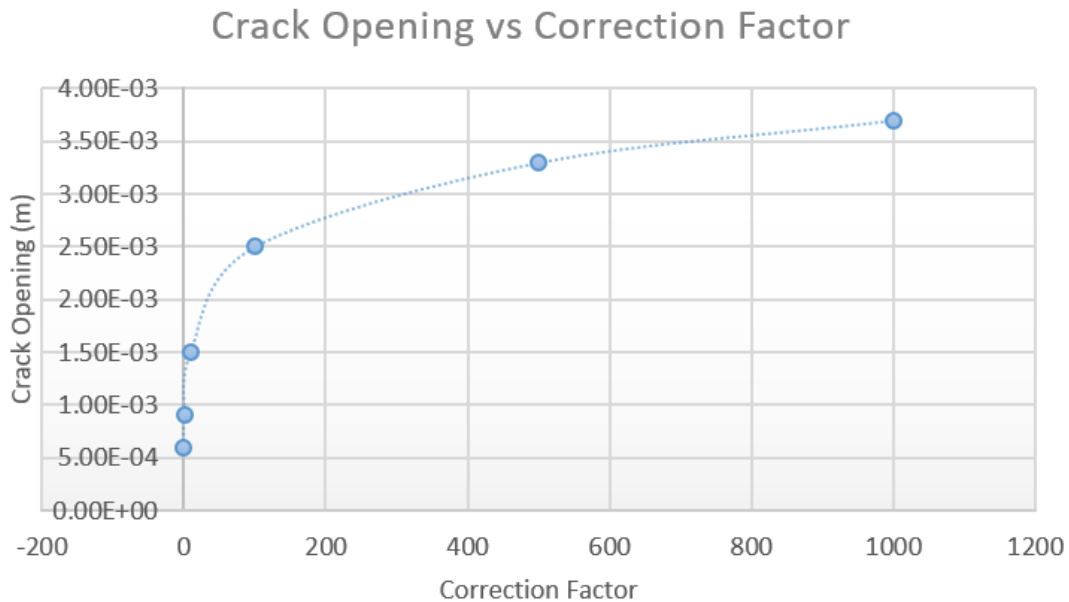


Figure 3.3: The results of varying correction factor, γ over four orders of magnitude. Above we see the inverse relation between the crack opening and the correction factor- as γ increases, the crack opening increases. Below we see the strong inverse relation between the effective permeability and the correction factor - as the correction factor increases, the permeability decreases.

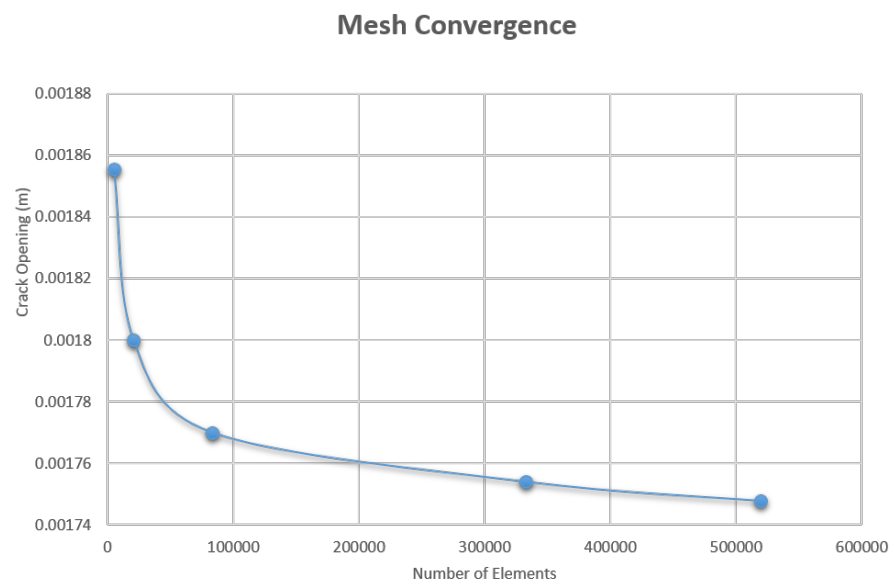


Figure 3.4: As we decrease the mesh parameter h , we approach $1.74 \cdot 10^{-3}$, which is the analytical solution to this problem.

where $2 \cdot c_0$ is the initial length of crack before growth. To verify the calculated crack opening as a function of pressure we compare (3.2) with our computed solutions over several mesh refinements. Because we are working with hexahedral elements, we effectively cast the 3D domain into a plane strain case by setting up a sheet of 8-node hexahedral elements and restraining displacements in the Z-direction, in the same setup as the mesh convergence study. We impose quarter symmetry boundary conditions by constraining the bottom portion and left portion of the mesh with the appropriate Dirichlet boundary conditions in c and \mathbf{u} , and enforcing $p = 0$ on this same boundary. We introduce a mass flux boundary condition, $Q = 0.32 \frac{kg}{s \cdot m^2}$ on the side-set corresponding to $\Omega X [-8, 8]$ surface between with $Y = 0$, as shown in figure 3.4, finding that this particular mass flux provides a steady flow into the desired portion of the mesh where we wish a crack to form. After sufficient stress accumulates in this region of high pore pressures, the phase-field variable begins to decay. For $c < c_{crit}$, the critical stress is established at a corresponding pore pressure of $p_0(\mathbf{x})$ and we begin to measure the crack opening w within the damaged region, along with the pressure change at these locations, $p - p_0$. We assign $c_{crit} = 0.75$, allowing for a 25% decay in the phase-field variable per [6]. We monitor the crack opening magnitude, as calculated in (2.33) on the damaged portion of the mesh, noting the location from the center of the damaged area, $c_0 = 8m$ in our test, and compare these results to the analytical results from (3.2). Figure 3.5 shows that our calculation of the crack opening matches up very nicely with the analytical solution, and the central portion of the crack opening converges to the analytical solution, shown in the previous subsection.

It is clear from the figure that the numerical results are very much in line with the analytical solution towards, especially at the center of the crack. However, there is some disagreement toward the crack tips. These results are not surprising - with our model set up in a porous flow regime, the fluid pressures will not be bounded by the injection zone of length $2c_0 = 16$ and the crack will spread beyond the injection zone, as the data indicates. What is important is that the solution converges with mesh refinement in a crack volumetric sense. This is shown to be the case in the previous convergence study because the volume of a crack is directly related to the crack width as shown in the formula below [37].

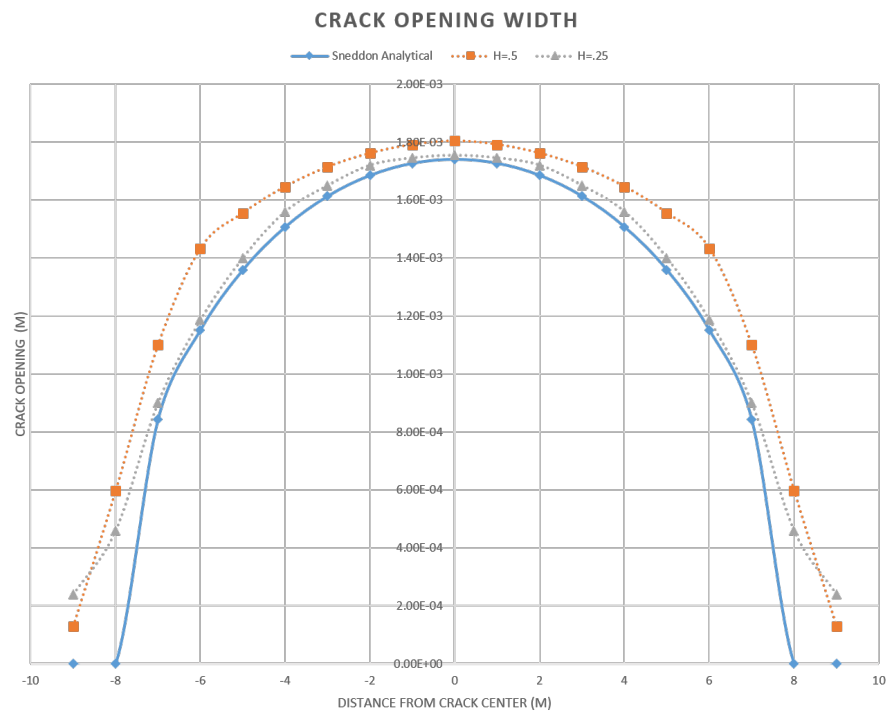


Figure 3.5: Results from crack opening benchmark. Simulation results of the aperture along a crack's profile that is driven by a constant pore pressure. Several different mesh refinements are compared against Sneddon's analytical solution.

$$V(x) = \frac{2\pi \cdot p \cdot c_0(1 - \nu^2)(1 - \frac{x^2}{c_0^2})^{\frac{1}{2}}}{E} \quad (3.3)$$

3.2.5 Mesh Alignment Study

In a final model verification test, we would also like to show that this model can resolve fractures that propagate regardless of the orientation of the elements on the mesh. We test this by injecting fluid into a mesh corner of sheet of hexahedral elements with boundary conditions that caused the fluid to travel in a diagonal direction, with fractures propagating at a 45 degree angle to the elements. The domain is discretized into 7200 hexahedral elements forming a 30 m x 30 m x 0.125 m sheet. We restrict the bottom surface of the mesh from displacements in X displacement, and the left surface of the mesh from displacements in Y, and introduce a flux into the corner elements where these two surfaces meet. Using the parameters in table 1, we use a length-scale of $l_0 = 0.5$ m and allow the test to run for 5 seconds, during which pressure builds in the injection zone until a fracture forms, along which the fluid flows.

Figure 3.6 shows this fracture propagating at a 45 degree angle through the elements for both cases: $l_0 = 0.5$. This test shows that the phase-field solution does not strongly follow specific mesh orientations, and cracks are able to propagate in directions that are not along elements' edges. The prior conclusions will be valid so long as the mesh size size is sufficiently small compared to the chosen length-scale.

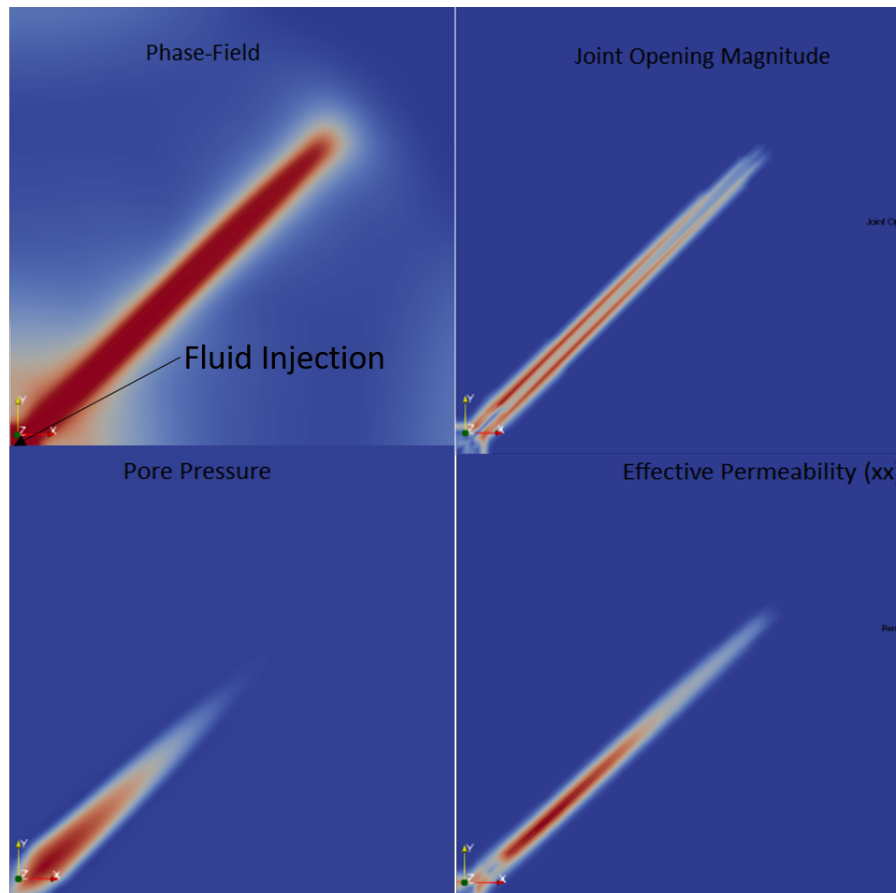


Figure 3.6: A fluid is injected into mesh as shown, with a crack propagating diagonally across the mesh's elements. The top left shows the phase-field representation of the fracture. The top right shows the crack opening associated with the fracture. The bottom left shows the pore pressure distribution along the fracture, and the bottom right shows the k_{xx} component of the effective permeability.

Chapter 4

Application and Results

4.1 Scope

The purpose of this section is to apply the previously described model to physical situations that we wish to explore. This model, along with the functionality of Aria, lends itself naturally to problems in geomechanics, which will be the focus of the following applications. In order to demonstrate the capabilities of this model, we consider incompressible fluid flow in the subsurfaces, particularly injection into materials with realistic, rock-like mechanical properties. In the following numerical experiments we adopt the material and geometric parameters shown in table 3.1, unless otherwise noted. These parameters are chosen to be representative of average limestones, and are similar to those used in [11]. In order to ensure that we select a meaningful length scale parameter, we compute $l_0 = 0.04$ m from these parameter values and following [43] we assign a mesh size $h = \frac{l_0}{2}$ in the areas of the domain where we would like to provide proper resolution for a brittle fracture.

4.1.1 Description of Computational Domain

This domain could be made to represent any arbitrary depth by applying a uniform pressure representing the overburden to the top of the green layer shown in figure 4.1. In these studies, we take this to be the earth's surface, and no such pressure is applied, but rather, we restrain displacements of this surface in the Z direction. We consider domains with four-fold symmetry that are 20 m x 20 m x 20m, with varying injection areas, which are depicted as orange and red in figure

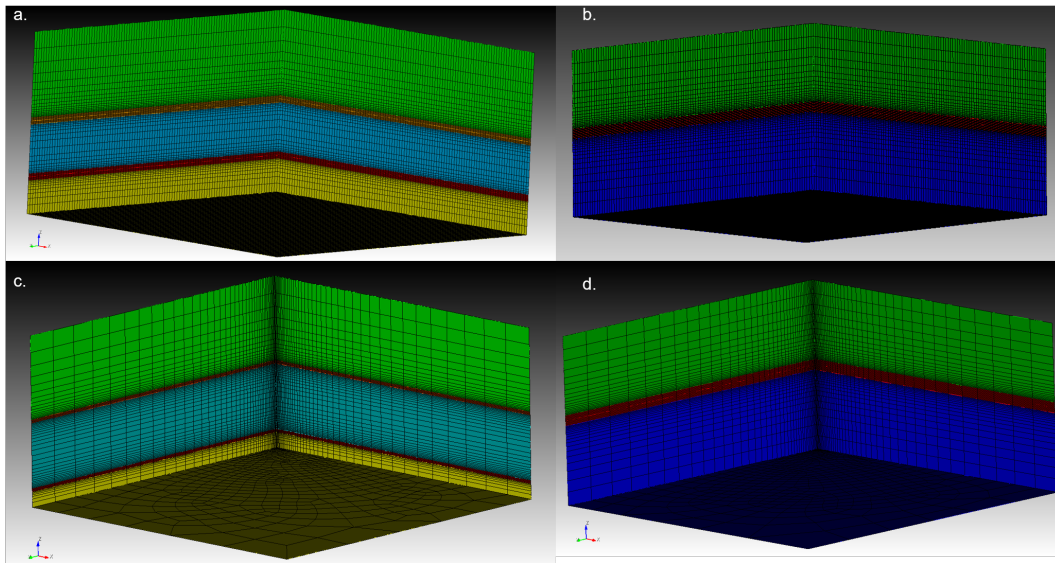


Figure 4.1: Discretization of the quadrant-domains into hexahedral elements with biasing in the Z direction refining the areas we expect to see fractures. The top meshes show around 620,000 elements, while those on the bottom show around 33,000.

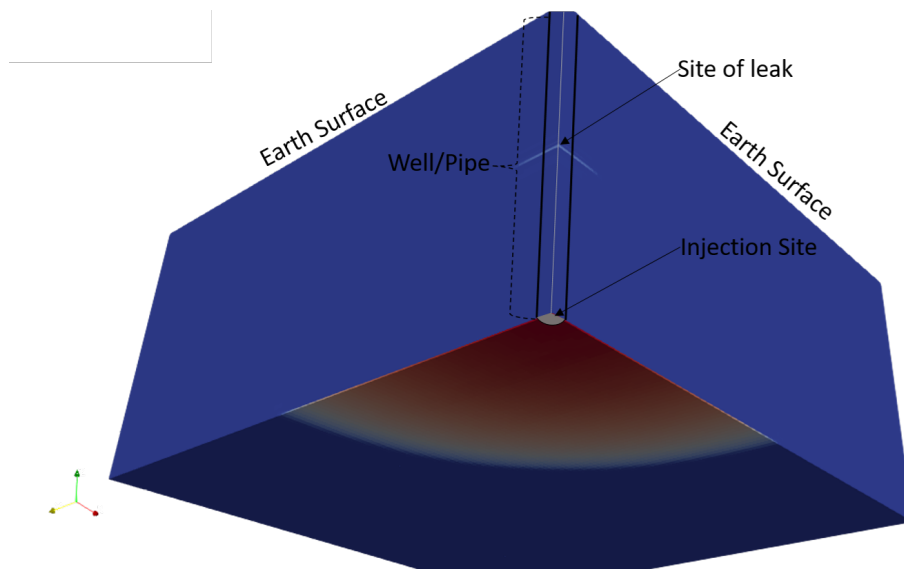


Figure 4.2: The setup for the first application is shown here. An injection well/pipe extends from the earth's surface down to the intended injection site. The figure also shows the resulting crack opening in the computational domain after 20 days.

4.1. The domains are biased away from these areas for computational thrift, being discretized into 620,000 hexahedral elements and are shown in a. and b. in figure 4.1. The bottom of this figure

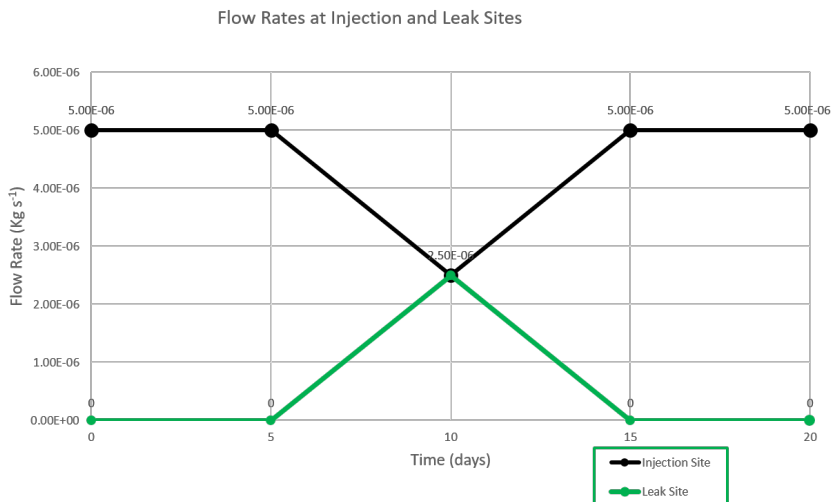


Figure 4.3: The flow rates for the injection site (blue) and the leak site (orange) are shown over the 20 day simulation. Here, a., b., c., and d. represent times $t = 5, 10, 15$ and 20 days respectively

shows more computationally efficient meshes, with about 34,000 elements. There were noticeable mesh dependencies that were magnified during the sharply transient portions of the simulations. Once the proper model parameters were tuned using the more efficient, heavily biased meshes, the same tests were run on the more refined mesh to produce cleaner results.

4.2 Geomechanics Setting

4.2.1 Problem Description

In our first application, we wish to model an isotropic porous subsurface of weak limestone lithography into which a fluid is injected over the course of time. Figure 4.2 depicts the physical set up of the problem. We consider a simulation time of 5 days, during which the viscous fluid is injected into subsurface limestone at a depth of 5 meters. The fluid and solid parameters are shown in table 3.1, with the exception of the fluid viscosity, which we take to be $\mu = 0.1 \text{ Pa}\cdot\text{s}$, and the intrinsic permeability, which is taken to be $k_{ii} = 1 \cdot 10^{-16} \text{ m}^2$. The injection areas form a

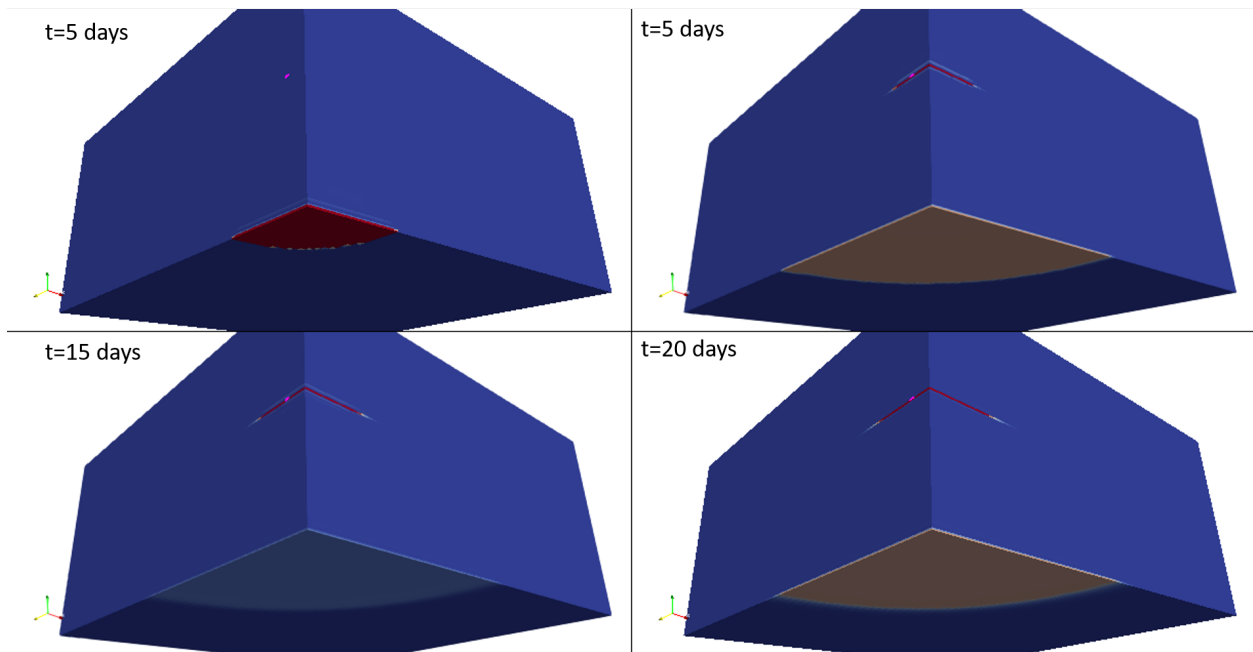


Figure 4.4: Pore pressure is ramped up at injection site until $t = 5$ days, at which time a leak forms, diverting flow until fully healed at $t = 15$ days, when full flow is returned to the injection site.

rectangle in the Z-plane of the orange and red layers closest to the viewer, forming an area on top of 15 elements and covering 0.64 m^2 , which approximates 0.45 m diameter pipe.

The simulation begins with the injection at an initial rate of $q_0 = 5 \cdot 10^{-6} \frac{\text{kg}}{\text{s}}$, into the subsurface with an initial time-step for both Aria and Adagio of $dt = 2000 \text{ s}$, or about 30 minutes. At time $t_1 = 5 \text{ days}$, the flow rate, q_0 is ramped down linearly in the injection area to represent pressure loss to a subsurface leak that is imposed in the pipe leading to the injection zone, while simultaneously causing a second flux to linearly ramp up at the site of the leak. This leads to a flow rate of $q_1 = 0.5 \cdot q_0$ applied at both the original injection area and the location of the leak at $t = 10 \text{ days}$, at which time the leak begins to heal. By $t = 15 \text{ days}$ the leak is fully repaired, diverting the full fluid flux back into the intended injection area. Figure 4.3 depicts the two flow rates at the leak and the injection site over time. This problem simulates the injection of fluids into the shallow subsurface, both purposeful and unintentional, and how the fluid pressure and fracture distributions evolve during this process. In order to capture the consequences of a leak in the pipe, we set the problem up with the mass flux boundary conditions in two locations, which vary over time. The repair of the leak could be attributed to microparticle accretion at the leak site.

4.2.2 Results and Discussion

As fluid begins to accumulate at the injection site 5 meters below the earth's surface, we begin to see an increase in fluid pressures around this depth. Because of the high fluid viscosity in this test, the permeability of the porous material does not play a key role in the fluid transport. Equation (2.39) indicates that the drop in porosity will cause an increase in the solid's deformation which will lead to displacements. Also, equation (2.31) tells us that the change in pore pressure will modify the effective stress. As this occurs, the phase-field variable evolves as a result of the increasing strains. At the critical value of $c = 0.75$, the crack opening w becomes non-zero, and the permeability jumps as a result. Because the permeability increases by orders of magnitude, equation (2.36) calls for a large jump in fluid velocities in the direction of the local pressure gradients, causing Poiseuille flow along the aptly damaged regions of the domain. The increased fluid pressure that

accumulates on the edges of the newly forming crack surface begins the whole process again, and the fracture spreads radially. This highly nonlinear, coupled physical process is the basis for the verification tests in subsection 3.2.1.

At $t = 5$ days, the leak begins to form by imposing a new flux boundary condition and the same coupled process begins to occur at the leak depth of 2.5 m, with the flux ramping up and depositing fluid at this depth. It should be noted that the leak at this depth is not due to crack nucleation that we are modeling in the pipe, but rather as a result of a rupture that is being imposed. During $t = 10 - 15$ days the leak is gradually repaired, by some unspecified process, and the fluid pressures are diverted back down to the intended injection site. The crack growth at the leak site was minimal, and as the pressures are relieved from the area the crack stops propagating, as expected. Figure 4.4 shows the evolution of the pore pressure over time, as described. The pore pressures remain highest in the leak site at the end of the simulation because the fracture volume is small compared to the volume at the lower injection site, where the fluid is free to spread throughout the crack. As time progresses, the fluid pressure, crack opening and permeability at the injection site lessen as the fractured area increases and fluid pressures are distributed.

Figure 4.5 shows the phase-field variable at the same four times. It shows that the fracture propagates in a radial pattern, forming a penny-shaped fracture front. The crack opening displacements over time are shown on the bottom of this same figure, with a maximum displacement at the center of the injection area, with the displacements decreasing radially to zero at the crack front. This result tells us that the highly damaged areas that have undergone the greatest strains and displacements will have the greatest fracture apertures. The effective permeability is dictated by equation (2.38), and will simply be a scaling of the crack opening figure. The maximum fluid pressure observed was 2.1 MPa, occurring at $t = 1.6$ days, which produced the conditions for the critical stress just as the fracture begins to form as indicated by the phase-field variable descending to $c = 0.75$. The maximum crack opening displacement is measured to be 1.6 mm, occurring at the injection site, at $t = 20$ days. We observe two penny shaped fractures at the end of the simulation. The shallower exists in the Z-plane at 2.5 m depth, with a radius of 1.14 m coinciding with the

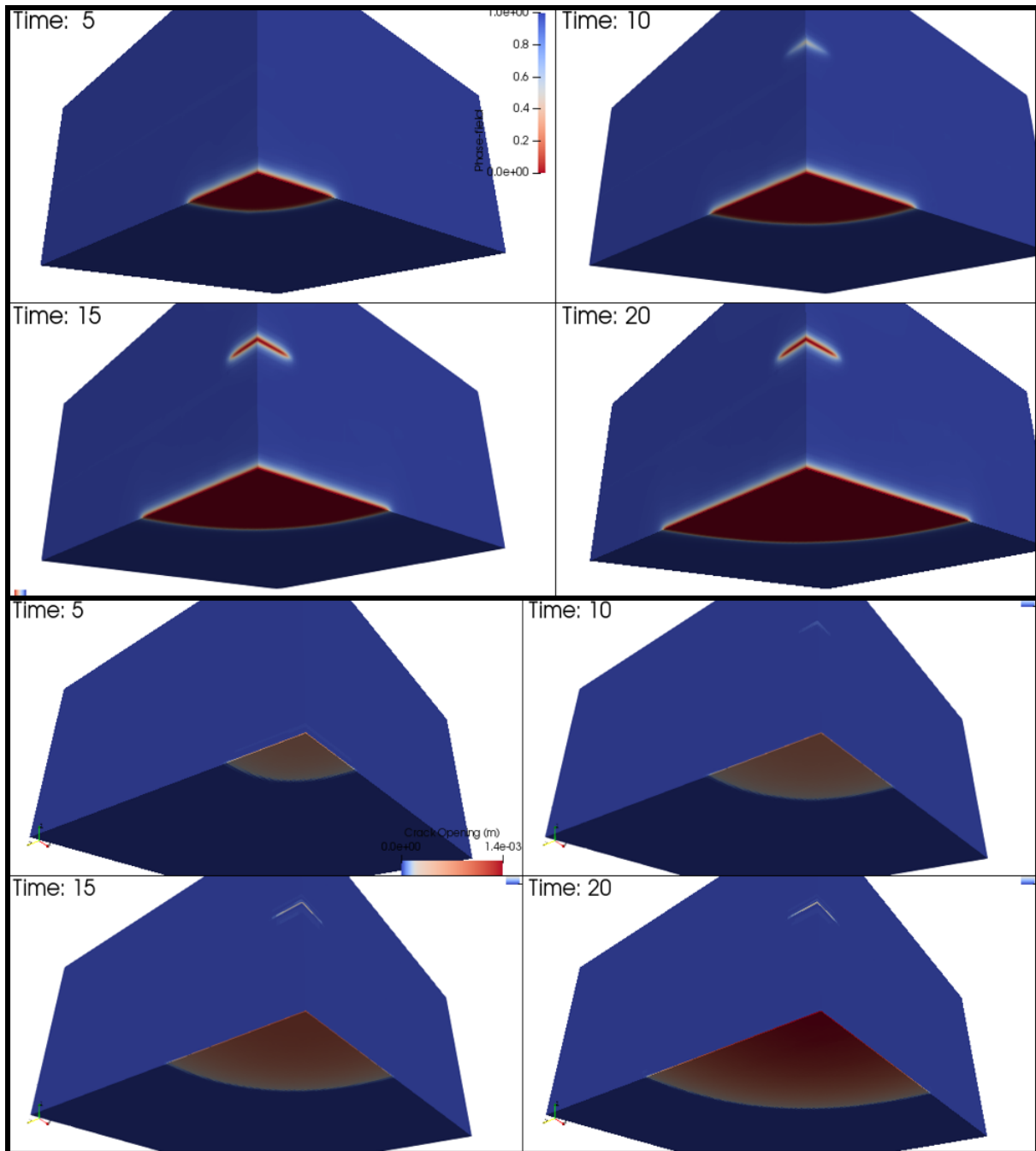


Figure 4.5: The phase-field variable (above) and the crack opening displacements (below) are shown evolving over the course of 20 days throughout the geomechanics simulation.

leak, and stopped evolving at a time of $t = 15$ days, however, locally high fluid pressures remained at this depth thereafter. The more prominent fracture is at a depth of 5 m in the Z-plane, at the injection site, which has continued to evolve throughout the entire simulation, and grew to a final radial length of 4.48 m at 20 days.

This application can be easily extended to many other geomechanical modeling problems, involving differing fluids, rock types and time-scales. Examples would include wastewater injection into aquifers and modeling of fractures in nuclear containment vessels. Future work will concentrate on dealing with multi-phase fluids over very long timescales, with pre-existing fractures introduced, that can be further propagated using this coupled modeling approach. Applications in CO₂ sequestration and wastewater injection are also excellent extensions of this type of simulation.

It should be noted that similar results in terms of fluid pressure distributions, crack opening displacements, and phase-field solutions were captured with water as the injected fluid, most notably the viscosity at $\mu = 1 \cdot 10^{-3}$ Pa s. In order to generate fractures in this scenario, a simulation time of 20 seconds, rather than 5 days, was used, along with injection rates that were 5 orders of magnitude higher. Figure 4.6 shows the pore pressure distributions after 5 days of injection at a rate of $q = 10^{-6}$ kg/s, with a viscosity of $\mu = 0.1$ on the left, and $\mu = 0.001$ Pa s on the right. With the more viscous fluid, we see a fracture toughness dominating regime, where fracture has formed, and the fluids distribute along it. With the less viscous case, we see a porous flow dominating regime, where the fluids diffuse through the permeable rock skeleton. This tells us that viscosity plays a very important role in the time-scale over which we can observe fracture. The reason for this is discussed in the following section.

4.3 Sensitivity of Parameters

4.3.1 Motivation and Description

Because of the extreme spatial and temporal ranges involved in the modeling of fluid flow and fracture within porous media, we must focus on relatively short timescales during which high fluxes

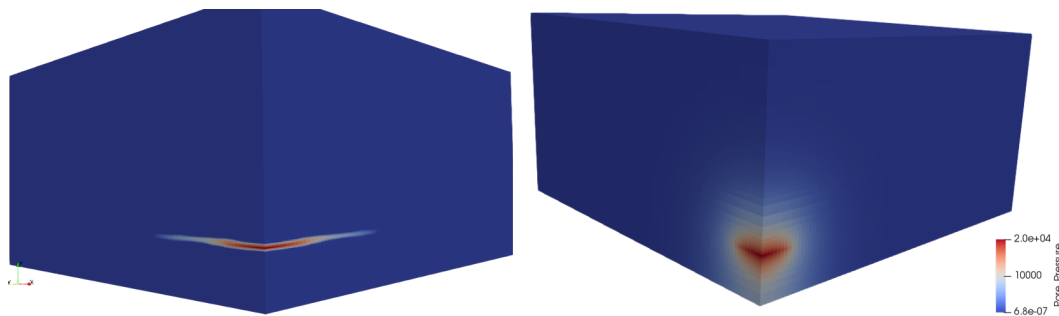


Figure 4.6: Fluid pressures are shown after roughly 5 days of injecting a highly viscous fluid (left) where fracture and Poiseuille flow dominate, and a fluid with the viscosity of water (right), where diffusion and porous flow dominate.

of fluids are introduced when using a less viscous fluid such as CO_2 or water. We would like to prevent the previously mentioned sharp transients that are associated with very high injection rates required to overcome the porous flow away from an injection site that are associated with common permeability values of rock. In order to do this, we would only observe the onset of fracture with relatively slow flux scenarios of highly viscous fluids, or fast flux scenarios with water or similarly low viscous fluid injections. If the prescribed injection rate is relatively slow and applied over a long period of time, the diffusive flow away from the high pressure will dominate the fluid transport, and no cracks will form. In other words, for any chosen porous flow regime, there is a minimum injection rate that acts as a threshold flux value determining whether or not fractures will form and propagate through such a medium. From observation, for a given injection rate Q , the parameters \mathbf{k} , μ and E most strongly affect the growth of the phase-field variable. More discussion surrounding the two competing storage mechanisms, porous and Poiseuille flow, within elastic porous media can be found in [16].

In order to understand the parameters that affect the a fluid's ease of fracturing a solid more clearly, we will use our model to perform a sensitivity study with the previously mentioned parameters that most directly dictate the fluid velocity. Equation (2.36) is repeated below to remind the reader of the relationship between Darcy velocity and the two parameters of interest:

$$\mathbf{v} = -\frac{\mathbf{k}}{\mu} \cdot (\nabla p - \rho_f \mathbf{g}) \quad (4.1)$$

During this study we fix the fluid and solid material parameters to those in table 3.1, and inject at a rate of $q = 5 \cdot 10^{-2}$ kg/s while observing crack formation and growth. We choose extreme values for the parameters of interest, and vary in between these values while keeping the other parameters of interest fixed at a reasonable value, which happen to be $k = 10^{-15} \text{ m}^2$, $\mu = 10^{-3} \text{ Pa s}$ and $E = 3 \cdot 10^{10} \text{ Pa}$. We wish to measure the ease at which the solid-fluid regime will fracture, which is achieved by recording the time it takes for a fracture to form, that is for the phase-field variable to reach a critical value of $c \leq 0.75$.

4.3.2 Results

The values for the intrinsic permeability components considered for this study ranged from 0, representing impermeable, up to 10^{-13} . The lower bound produced a fracture very quickly - after 3 seconds of fluid pressure, the pore pressure increased to values that lead to fracture. The upper bound was dictated by the porous flow dominating the physics, preventing ample buildup of pressures for the selected injected rate to produce a fracture. Figure 4.7 shows the result, with intrinsic permeability along the X axis, and the time to generate fracture on the vertical axis. As we would expect, increasing permeability has drastic effect increasing effect on the ease of fracture, with what appears to be a quadratic relationship between the time to fracture and k .

On the bottom of this figure, the results of the viscosity sensitivity are shown. A lower bound of $5 \cdot 10^{-4}$ was chosen, which is half that of liquid water at typical surface temperatures, and an upper bound of 10^{-2} was chosen, as it caused fracture after the first time-step. There appears to be a hyperbolic relationship between the time to fracture onset and the viscosity, with very sudden change as the viscosity drops below 10^{-3} and quickly approaching near immediate fracture as the value is increased beyond $\mu \approx 5 \cdot 10^{-3}$, making it an extremely sensitive parameter in this coupling. We see that this hyperbolic relationship has a physical origin stemming from equation (4.1), with μ being in the denominator, driving fluid velocities to infinity when μ approaches zero.

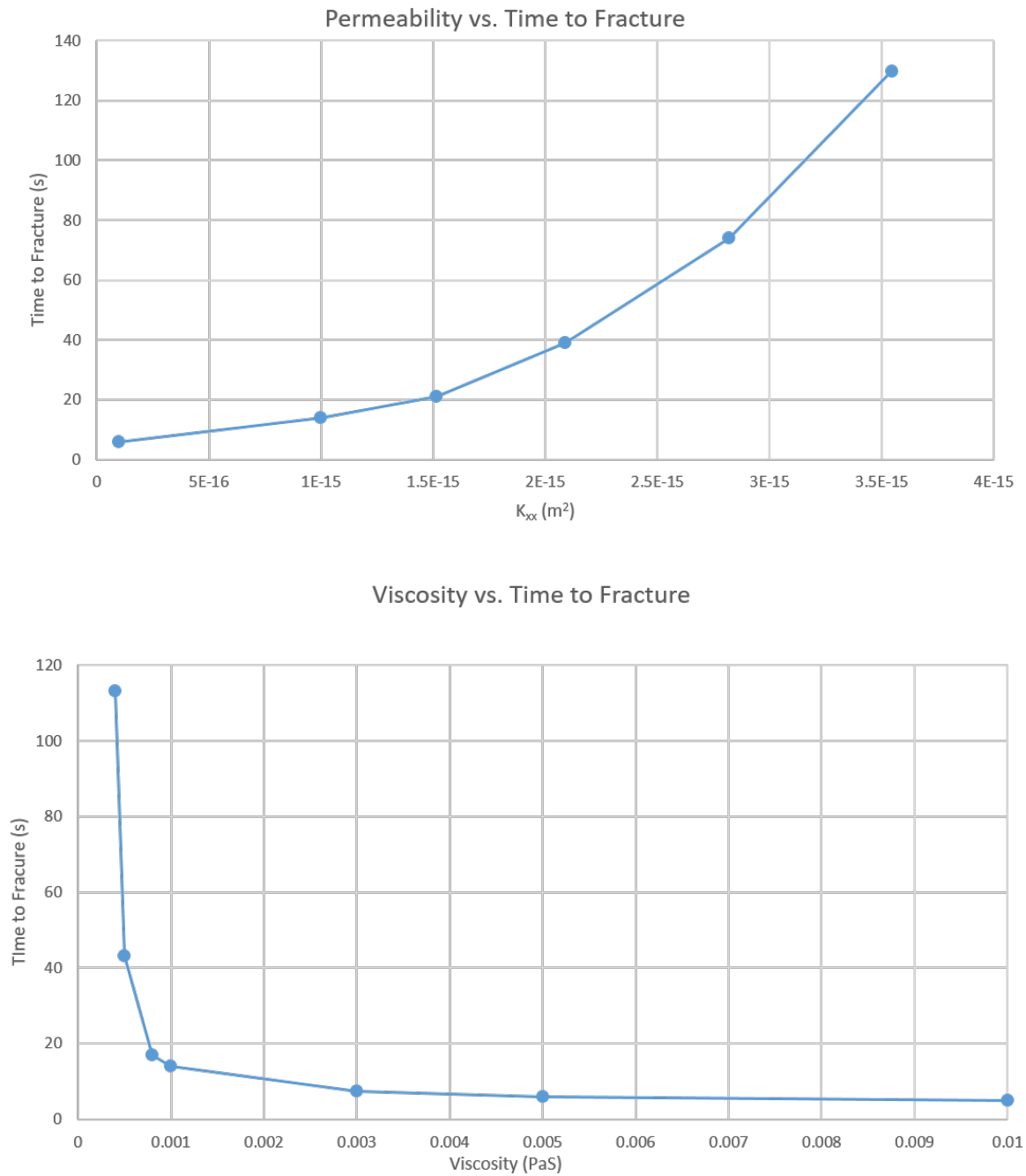


Figure 4.7: Plot of time to fracture initiation as a function of varying intrinsic permeability (above), and varying fluid viscosity (below).

An engineering insight from these results tells us that porous flow scenarios with highly impermeable materials or highly viscous fluids will have a tendency to develop fractures much easier than their counterparts. If the goal is to avoid subsurface cracking during injection into an aquifer with a given permeability, it would be advisable to keep the fluid's viscosity as low as possible, by perhaps mixing in an appropriate additive.

Figure 4.8 shows the results of the varying Young's modulus and its relation to the critical stress at fracture onset. We observe a response that is analogous to equation (2.29), with the critical stress growing proportionally to the square root of the material's Young's modulus. During this parameter study, fluid was injected under the same conditions as the previous test, only holding both the permeability and viscosity at values that are consistent with limestone and water. Rather than monitoring the time to fracture, the critical stress was recorded, which, by definition occurs when the phase-field variable reaches 0.75, as this marks the onset of fracture. An interesting non-linearity arises when changing the Young's modulus variable, in the sense that we should also be adjusting our fracture length-scale variable per equation (2.30). This was taken into account during the tests and adjusted accordingly.

In the preceding applications, we assume a lack of initial flaws in the porous solid, which is highly unphysical. In fact, these flaws, which are present at many scales in all real materials, are often the source of fracture nucleation [3]. In future work we will include such flaws to more accurately capture a more physically accurate situation, but including a distribution of initial Young's modulus and phase-field values across the domain.

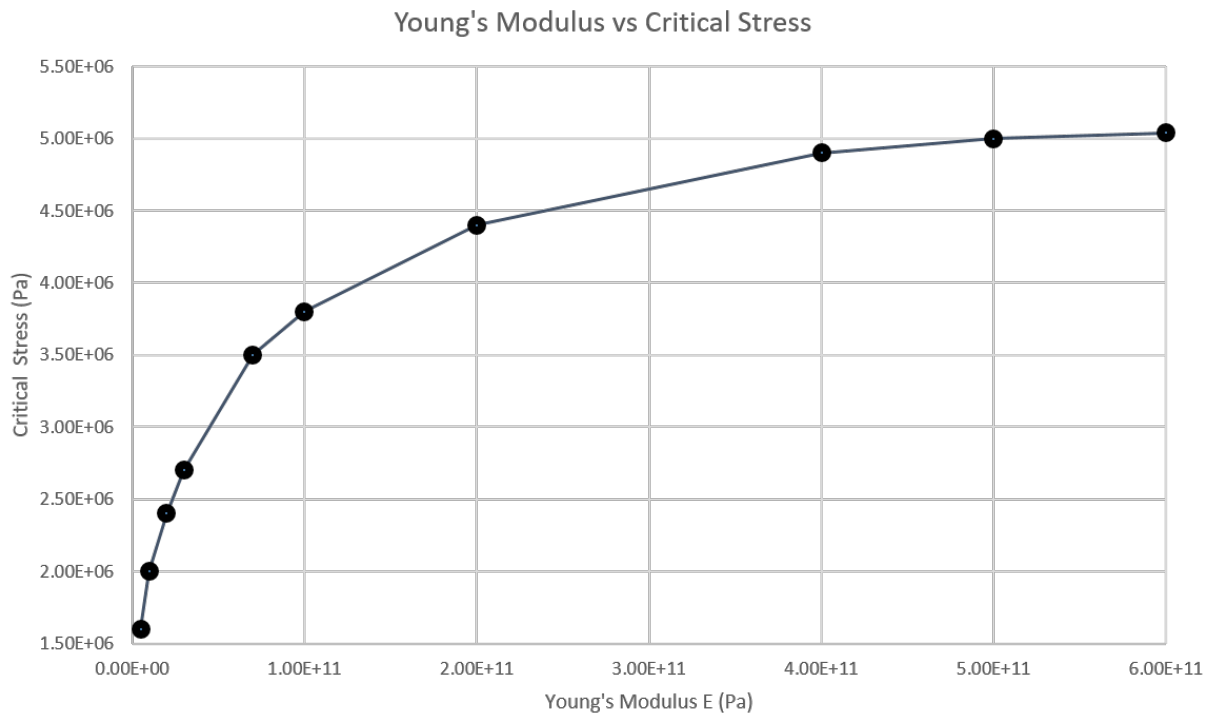


Figure 4.8: Plot of time to fracture initiation as a function of varying Young's Modulus.

Chapter 5

Conclusions and Discussions

The coupled physics of fluid-driven fracture, and the resulting flow in porous media must be simulated in a framework that can accurately capture the solid and fluid mechanical problems on hand. Phase-field modeling of fractures offers the convenience of capturing fracture formation without *a priori* knowledge of the location using a variational approach, and provides a means to calculate crack opening displacements. These displacements may be used to augment a material's effective permeability using the cubic law from lubrication theory, driving fluid pressures to distribute within cracked portions of the domains.

The Sierra module Aria provides a powerful environment to explore geomechanics simulations, and when used in conjunction with the solid module Adagio, the phase-field material model is available to provide the two-way coupling that is useful to model scenarios where evolving fluid pressures and fractures may interact. Our objective was to show that this coupled physics model accurately calculates crack opening displacements, and can provide useful insight into geomechanics applications such as fluid injection scenarios. Several verification tests show that the model behaves as predicted, including mesh convergence and benchmark studies.

An application of the model shows how a leaking injection bore-hole might distribute fluids into the subsurface, monitoring the results of both intended and unintentional injections. We applied the model to a parameter sensitivity analysis under rock-like values where the model was used to explore some of the effects of the more sensitive fluid and solid material properties on the ease of fracture in fluid-driven poro-elastic regimes. One takeaway from this study is that $\frac{k_{ii}}{\mu}$ must

be sufficiently small compared to the injection rate Q in order to see fracture genesis. This model can provide engineering insight to the possibility of fracture formations in known geological settings, which allows proper selection of a geologic site and fluid viscosity to either avoid or encourage fractures.

There are many possibilities for further development and future work with this modeling technique. Studying the existence of pre-existing fractures within subsurfaces over long time periods and use of multi-phase flow capabilities, thermal coupling and water-gas-brine mixtures are all readily available within Aria's toolkit. Extension of the correction factor as a function of crack opening should be considered to more accurately modify the effective permeability. Additional use of this model will also consider the distribution of initial flaws in materials, to more accurately capture the process of fracture nucleation.

Bibliography

- [1] Luigi Ambrosio and Vincenzo Maria Tortorelli. Approximation of functional depending on jumps by elliptic functional via tconvergence. Communications on Pure and Applied Mathematics, 43(8):999–1036.
- [2] K. Aziz and A Settari. Petroleum Reservoir Simulation. Dover Civil and Mechanical Engineering. Applied Science Publishers, 1979.
- [3] Z. P. Bažant. Size effect on structural strength: a review. Archive of Applied Mechanics, 69(9):703–725, Nov 1999.
- [4] ZP Bazant and Li Y. Stability of cohesive crack model: Part i– energy principles. Journal of Applied Mechanics, 62(4):959–964, 1995.
- [5] M. A. BIOT and G. Temple. Theory of finite deformations of porous solids. Indiana University Mathematics Journal, 21(7):597–620, 1972.
- [6] Michael J. Borden, Thomas J.R. Hughes, Chad M. Landis, Amin Anvari, and Isaac J. Lee. A phase-field formulation for fracture in ductile materials: Finite deformation balance law derivation, plastic degradation, and stress triaxiality effects. Computer Methods in Applied Mechanics and Engineering, 312:130 – 166, 2016. Phase Field Approaches to Fracture.
- [7] Michael J. Borden, Clemens V. Verhoosel, Michael A. Scott, Thomas J.R. Hughes, and Chad M. Landis. A phase-field description of dynamic brittle fracture. Computer Methods in Applied Mechanics and Engineering, 217220:77 – 95, 2012.
- [8] Michael Johns Borden. Isogeometric analysis of phase-field models for dynamic brittle and ductile fracture. PhD Thesis, 2012, The University of Texas, Austin, TX.
- [9] Blaise Bourdin, Gilles Francfort, and J.-J Marigo. The variational approach to fracture. 91:5–148, 04 2008.
- [10] G.T. Camacho and M. Ortiz. Computational modelling of impact damage in brittle materials. International Journal of Solids and Structures, 33(20):2899 – 2938, 1996.
- [11] Anozie Ebigbo, Holger Class, and Rainer Helmig. Co2 leakage through an abandoned well: problem-oriented benchmarks. Computational Geosciences, 11(2):103–115, Jun 2007.
- [12] Bernd Flemisch, Alessio Fumagalli, and Anna Scotti. A Review of the XFEM-Based Approximation of Flow in Fractured Porous Media, pages 47–76. Springer International Publishing, Cham, 2016.

- [13] Foster, J. T., Silling, S. A., and Chen, W. W. State based peridynamic modeling of dynamic fracture. DYMAT - International Conference on the Mechanical and Physical Behaviour of Materials under Dynamic Loading, 2:1529–1535, 2009.
- [14] A. A. Griffith. The phenomena of rupture and flow in solids. Philosophical Transactions of the Royal Society of London A: Mathematical, Physical and Engineering Sciences, 221(582-593):163–198, 1921.
- [15] H. Hall. Compressibility of reservoir rocks. Journal of Petroleum Technology, 5(1):17–19, Jan 1953.
- [16] J. Hu and D. I. Garagash. Plane-strain propagation of a fluid-driven crack in a permeable rock with fracture toughness. Journal of Engineering Mechanics, 136(9):1152–1166, 2010.
- [17] T.J.R. Hughes. The Finite Element Method: Linear Static and Dynamic Finite Element Analysis. Dover Civil and Mechanical Engineering. Dover Publications, 2012.
- [18] A. R. Khoei, O. R. Barani, and M. Mofid. Modeling of dynamic cohesive fracture propagation in porous saturated media. International Journal for Numerical and Analytical Methods in Geomechanics, 35(10):1160–1184, 2011.
- [19] Jaehong Kim, Wei Wang, and Richard A. Regueiro. Hybrid time integration and coupled solution methods for nonlinear finite element analysis of partially saturated deformable porous media at small strain. International Journal for Numerical and Analytical Methods in Geomechanics, 39(10):1073–1103.
- [20] Toshiyuki Koyama. Phase Field Approach, pages 1091–1115. Springer Berlin Heidelberg, Berlin, Heidelberg, 2011.
- [21] Christopher J. Larsen. Models for dynamic fracture based on griffith’s criterion. In Klaus Hackl, editor, IUTAM Symposium on Variational Concepts with Applications to the Mechanics of Materials, pages 131–140, Dordrecht, 2010. Springer Netherlands.
- [22] Sanghyun Lee, Andro Mikelic, Mary F. Wheeler, and Thomas Wick. Phase-field modeling of proppant-filled fractures in a poroelastic medium. Computer Methods in Applied Mechanics and Engineering, 2016.
- [23] Eric Lorentz, S. Cuvilliez, and K. Kazymyrenko. Convergence of a gradient damage model toward a cohesive zone model. Comptes Rendus Mecanique, 339(1):20 – 26, 2011.
- [24] M.J. Martinez, P. Newell, J.E. Bishop, and D.Z. Turner. Coupled multiphase flow and geomechanics model for analysis of joint reactivation during co2 sequestration operations. International Journal of Greenhouse Gas Control, 17:148–160, 2013.
- [25] SIERRA Solid Mechanics Team Computational Solid Mechanics and Structural Dynamics Department Engineering Sciences Center. SIERRA Code Coupling Module: Arpeggio User Manual Version 4.44, April 2017.
- [26] Christian Miehe, Martina Hofacker, and Fabian Welschinger. A phase field model for rate-independent crack propagation: Robust algorithmic implementation based on operator splits. Computer Methods in Applied Mechanics and Engineering, 199(4548):2765 – 2778, 2010.

- [27] Christian Miehe and Steffen Mauthe. Phase field modeling of fracture in multi-physics problems. part iii. crack driving forces in hydro-poro-elasticity and hydraulic fracturing of fluid-saturated porous media. Comput. Methods Appl. Mech. Engrg, 304:619–655, 2015.
- [28] Andro Mikeli, Mary F Wheeler, and Thomas Wick. A quasi-static phase-field approach to pressurized fractures. Nonlinearity, 28(5):1371, 2015.
- [29] Nicolas Mos, John Dolbow, and Ted Belytschko. A finite element method for crack growth without remeshing. International Journal for Numerical Methods in Engineering, 46(1):131–150, 1999.
- [30] David Mumford and Jayant Shah. Optimal approximations by piecewise smooth functions and associated variational problems. Communications on Pure and Applied Mathematics, 42(5):577–685.
- [31] Patrick K. Notz, Samuel R. Subia, Matthew M. Hopkins, Harry K. Moffat, David R. Noble, and Tolulope O. Okusanyar. SIERRA Multimechanics Module: Aria User Manual Version 4.40, Sandia Technical Report May 2016.
- [32] V. I. Osipov. Physicochemical theory of effective stresses in soils. Water Resources, 41(7):801–818, Dec 2014.
- [33] G. Rastiello, C. Boulay, S. Dal Pont, J.L. Tailhan, and P. Rossi. Real-time water permeability evolution of a localized crack in concrete under loading. Cement and Concrete Research, 56:20–28, 2014.
- [34] H. A. F. A. Santos and V. V. Silberschmidt. Finite Element Modelling of 2D Brittle Fracture: The Phase-Field Approach, pages 1–21. Springer International Publishing, Cham, 2015.
- [35] Ryan Shaw, Anthony M. Agelastos, and Joel D. Miller. Guide to Using Aria, Sandia Technical Report March 2015.
- [36] S.A. Silling and E. Askari. A meshfree method based on the peridynamic model of solid mechanics. Computers & Structures, 83(1718):1526 – 1535, 2005. Advances in Meshfree Methods.
- [37] I. N. Sneddon. The distribution of stress in the neighbourhood of a crack in an elastic solid. Proc. R Soc London A, 187:229–260, 1946.
- [38] David T. Snow. Anisotropic permeability of fractured media. Water Resources Research, 5(6):1273–1289.
- [39] Samuel R. Subia, James R. Overfelt, and David G. Baur. Sierra/SolidMechanics 4.46 Users Guide, September Sandia Technical Report 2017.
- [40] Karl Terzaghi. Erdbaumechanik auf bodenphysikalischer Grundlage. F. Deuticke, 1925.
- [41] Julien Vignollet, Stefan May, René de Borst, and Clemens V. Verhoosel. Phase-field models for brittle and cohesive fracture. Meccanica, 49(11):2587–2601, Nov 2014.
- [42] M.F. Wheeler, T. Wick, and W. Wollner. An augmented-lagrangian method for the phase-field approach for pressurized fractures. Computer Methods in Applied Mechanics and Engineering, 271:69 – 85, 2014.

- [43] Xue Zhang, Chet Vignes, Scott W. Sloan, and Daichao Sheng. Numerical evaluation of the phase-field model for brittle fracture with emphasis on the length scale. Computational Mechanics, 59(5):737–752, May 2017.